J. Fluid Mech. (2012), *vol.* 691, *pp.* 279–314. © Cambridge University Press 2011
doi:10.1017/jfm.2011.474

Sediment-laden fresh water above salt water: linear stability analysis

P. Burns and E. Meiburg†

Department of Mechanical Engineering, University of California, Santa Barbara, CA 93106, USA

(Received 19 May 2011; revised 30 August 2011; accepted 24 October 2011;
first published online 5 December 2011)

When a layer of particle-laden fresh water is placed above clear, saline water, both Rayleigh–Taylor and double diffusive fingering instabilities may arise. For quasi-steady base profiles, we obtain linear stability results for such situations by means of a rational spectral approximation method with adaptively chosen grid points, which is able to resolve multiple steep gradients in the base state density profile. In the absence of salinity and for a step-like concentration profile, the dominant parameter is the ratio of the particle settling velocity to the viscous velocity scale. As long as this ratio is small, particle settling has a negligible influence on the instability growth. However, when the particles settle more rapidly than the instability grows, the growth rate decreases inversely proportional to the settling velocity. This damping effect is a result of the smearing of the vorticity field, which in turn is caused by the deposition of vorticity onto the fluid elements passing through the interface between clear and particle-laden fluid. In the presence of a stably stratified salinity field, this picture changes dramatically. An important new parameter is the ratio of the particle settling velocity to the diffusive spreading velocity of the salinity, or alternatively the ratio of the unstable layer thickness to the diffusive interface thickness of the salinity profile. As long as this quantity does not exceed unity, the instability of the system and the most amplified wavenumber are primarily determined by double diffusive effects. In contrast to situations without salinity, particle settling can have a *destabilizing* effect and significantly increase the growth rate. Scaling laws obtained from the linear stability results are seen to be largely consistent with earlier experimental observations and theoretical arguments put forward by other authors. For unstable layer thicknesses much larger than the salinity interface thickness, the particle and salinity interfaces become increasingly decoupled, and the dominant instability mode becomes Rayleigh–Taylor-like, centred at the lower boundary of the particle-laden flow region.

Key words: double diffusive convection, ocean processes, sediment transport

1. Introduction

While it has been estimated that $O(10^9)$ tons of sediment are transported from rivers into the oceans every year (Milliman & Syvitski 1992), the processes by which this sediment settles out from usually buoyant river plumes are still poorly

† Email address for correspondence: meiburg@engineering.ucsb.edu

https://doi.org/10.1017/jfm.2011.474 Published online by Cambridge University Press

understood. Gaining insight into the dominant mechanisms will help determine the location of sediment deposits on the sea floor, which in turn represents important information for predicting the location of certain hydrocarbon reservoirs (Weimer & Slatt 2007; Meiburg & Kneller 2010). Currently, most oceanographic sedimentation models rely on Stokes settling as the main means of sediment transfer out of plumes (e.g. Henniger, Kleiser & Meiburg 2010), with some including flocculation effects (Syvitski *et al.* 1985; Hill *et al.* 1998). In recent years, more complex flow phenomena have been addressed as well, such as turbulence-enhanced settling (Aliseda *et al.* 2002; McCool & Parsons 2004; Bosse, Kleiser & Meiburg 2006), double diffusive sedimentation (Green 1987; Hoyal, Bursik & Atkinson 1999*a*; Parsons & Garcia 2000) and convective settling (Hoyal, Bursik & Atkinson 1999*b*; Maxworthy 1999; Parsons, Bush & Syvitski 2001) processes.

Sediment-laden riverine outflows into the ocean can be classified as either hypopycnal or hyperpycnal currents. A hypopycnal current is one in which the combined density of the fresh water and sediment suspended in the river is less than the density of the salty ocean water, resulting in the river outflows spreading along the top of the ocean. Alternatively, a hyperpycnal current is one in which the combined density of the river is more than that of the ocean, so that the river flow follows the sea floor. Such dense outflows are rare in nature, but can be very important to the overall sediment record of the deep ocean (Parsons *et al.* 2001). The present investigation focuses on hypopycnal currents, and more specifically on the instabilities that can arise from such density configurations. This configuration is sketched in figure 1, which shows the initially stably stratified system due to a larger salinity loading of the ocean as compared to the particle loading. After some time, the sediment particles can settle into the upper region of the saline layer and form an unstable layer at the top of the saline region.

There have been numerous experimental studies concerned with the instabilities generated at the lower interface of a surface density-driven current. By providing an analogy between sediment fingers and the better-known salt fingers, Green (1987) obtained estimates, in terms of sediment concentration and particle diameter, of the conditions under which the double diffusive flux of sediment should be important, as compared to the flux due to Stokes settling only. For a more in-depth review of salt fingers, the reader is directed to the papers by Turner (1967) and Stern (1969). Comprehensive overviews of the more general topic of double diffusive convection are provided in the book by Turner (1973) and the review article by Huppert & Turner (1981). Green (1987) reasons that, for sediment concentrations exceeding 100 mg kg^{-1}, the particle diameter should be less than 5 μm for the double diffusive flux to exceed the Stokes settling flux. Maxworthy (1999) investigated a similar set-up, but changed the stabilizing component from heat to salinity. His study focused on the conditions necessary for generating a bottom turbidity current through sedimentation from the buoyant river outflow. He defined a density difference ratio as the ratio of the stabilizing density difference between the ambient and interstitial fluid to the destabilizing density difference due to the sediment loading. The experiments demonstrated that, for values of this parameter near unity, the dynamics of the current were strongly dependent on the instabilities generated at the interface. Maxworthy attributed these instabilities to the growth of a dense layer of salty, particle-laden fluid similar to the sketch of figure 1, and believed the instabilities to be an extension of Rayleigh–Taylor theory. Parsons *et al.* (2001) performed a set of experiments similar to Green (1987) and Maxworthy (1999), but included both temperature and salinity as stabilizing components.

https://doi.org/10.1017/jfm.2011.474 Published online by Cambridge University Press

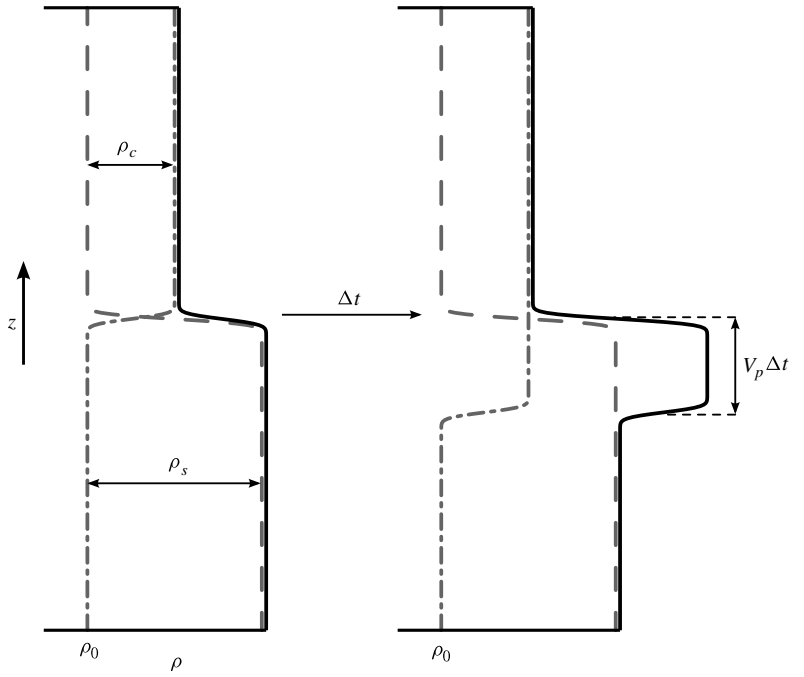


FIGURE 1. Sketch of density distributions for a buoyant river outflow showing the particle (dashed-dotted), salinity (dashed) and total density (solid) fields. The density of fresh water is indicated by ρ_0. The added density due to salinity, ρ_s, is greater than that due to particles, ρ_c, which results in an overall stable stratification. After some time Δt, the particles have settled downwards into the upper region of the saline layer, where they form an unstable layer of excess density whose lower boundary is gravitationally unstable. The thickness of this unstable layer is equal to the product of the settling velocity V_p and the elapsed time Δt.

The importance of the unstable layer was also discussed by Hoyal *et al.* (1999*a*) and Blanchette & Bush (2005). In both papers, the authors likened the growth of the unstable layer to the development of a thermal boundary layer in the heated-plate Rayleigh–Bénard problem, and consequently they defined a time-dependent Rayleigh number for the unstable layer. In Hoyal *et al.* (1999*a*), the authors used a threshold value for this Rayleigh number to create an expression for the finger width as $(1000\nu^2/g')^{1/3}$. The unstable layer has also been studied theoretically by Chandler (1998) and Redekopp (2002). The authors used linear theory to predict growth rates analytically for different unstable layer heights; however, they did not include a settling velocity or double diffusive effects in their calculations. The idea of boundary layer-driven convection is also seen in double diffusive systems. Linden & Shirtcliffe (1978) studied double diffusive convection in sugar-salt systems resulting from the formation of unstable boundary layers sandwiched around a stable diffusive core. These authors also applied a critical Rayleigh number criterion for the breakdown of the unstable boundary layers and the subsequent release of buoyancy into the fluid. However, the boundary layers of interest for Linden & Shirtcliffe (1978) were diffusively generated, while those of Hoyal *et al.* (1999*a*) and Blanchette & Bush (2005) were settling generated.

In addition to instabilities, other mechanisms affecting sedimentation have also been studied experimentally. McCool & Parsons (2004) studied sedimentation from

https://doi.org/10.1017/jfm.2011.474 Published online by Cambridge University Press

a stratified shear layer and found a positive correlation between turbulent energy and sedimentation rate. Their results showed an increase of as much as 50 % in sedimentation as compared to experiments of double diffusive sedimentation without turbulence. Revisiting the work of Blanchette & Bush (2005), the authors primarily focused on the effects of a spatially varying settling velocity. They found that hindered settling due to the increase in density across a salinity or temperature interface resulted in an increase in the particle concentration in the unstable layer, which in turn drove the convective instabilities.

While all of the above investigations provide insight into various important aspects of the stability of hypopycnal currents and stratified flows, the current investigation aims at enhancing our understanding of the role that particle settling plays in these mechanisms, especially with regard to the growth of double diffusive instabilities. For small settling velocities, we expect the instability to be driven by the diffusion of salinity, and to be very similar to double diffusive fingering with relatively small fingers dependent on the diffusivity ratio. For large settling velocities, we expect Rayleigh–Taylor structures to dominate instability, i.e. larger fingers that are independent of the diffusion of the salinity field. Section 2 outlines the physical problem, and defines the accompanying governing equations along with the relevant dimensionless parameters. The equations are linearized in § 3, and the stability problem is formulated as a numerical eigenvalue problem. The choice of numerical method, a rational spectral collocation approach, is discussed in detail in § 3, and convergence results are presented to support our choice of method. Section 4 focuses on the situation of settling particles in the absence of salinity, and it examines the physical mechanisms at play. A second, stabilizing component, here referred to as salinity, is introduced in § 5. Both convective instabilities as well as double diffusive effects are discussed. A summary of the findings is given in § 6.

2. Problem formulation

2.1. *Governing equations*

We consider the stability of an initially stationary, unbounded fluid with a vertically stratified density profile. The density is assumed to be a function of both the sediment concentration C and the salinity S. We start our analysis from the full Navier–Stokes equations

$$\boldsymbol{\nabla} \cdot \boldsymbol{u} = 0, \tag{2.1}$$

$$\rho \left(\frac{\partial \boldsymbol{u}}{\partial t} + \boldsymbol{u} \cdot \boldsymbol{\nabla} \boldsymbol{u} \right) = \mu \nabla^2 \boldsymbol{u} - \boldsymbol{\nabla} P + \rho \boldsymbol{g}. \tag{2.2}$$

Here, $\boldsymbol{u}$ denotes the fluid velocity, $\boldsymbol{g}$ the acceleration due to gravity, which is taken in the $-z$ direction, μ the dynamic viscosity and P the pressure. The density ρ is assumed to be a linear function in S and C,

$$\rho = \rho_0 (1 + \alpha S + \gamma C), \tag{2.3}$$

where ρ_0 represents the density of clear, fresh water and (α, γ) indicate the density expansion coefficients of salinity and sediment, respectively. In typical ocean environments, the density of salt water is ∼3–4 % above that of fresh water, which allows us to employ the Bousinessq approximation. Hence, ρ on the left-hand side of (2.2) can be replaced by ρ_0, and changes in density are considered important only as a source of buoyancy for the fluid. Salinity and sediment concentration are assumed to

https://doi.org/10.1017/jfm.2011.474 Published online by Cambridge University Press

be governed by the scalar transport equations

$$\frac{\partial S}{\partial t} + \boldsymbol{u} \cdot \boldsymbol{\nabla} S = D_s \nabla^2 S, \tag{2.4}$$

$$\frac{\partial C}{\partial t} + \boldsymbol{u} \cdot \boldsymbol{\nabla} C - V_p \frac{\partial C}{\partial z} = D_c \nabla^2 C. \tag{2.5}$$

Here, the D_i represent the dimensional diffusion coefficients for the scalars. The sediment diffusion coefficient can be derived from the Einstein–Stokes equation, and typically has values much smaller than the salinity diffusion coefficient. The dynamics of our problem would not change significantly if $D_c = 0$, but the resulting equations are easier to solve with a small, non-zero value. In (2.5), we assume that the sediment particles are dilute and have negligible inertia, so that they move with the sum of the fluid velocity and a superimposed settling velocity V_p pointing in the direction of gravity. For a detailed discussion of this Eulerian treatment of the particle concentration field, we refer the reader to Green (1987) and Necker *et al.* (2002). We furthermore assume that the particles are monodisperse and fall at a constant settling velocity, which depends on the particle size and shape. The non-zero value for the diffusion coefficient of the particles also models the smearing that may occur in a real suspension of particles as a result of a distribution of particle shapes and sizes, or of Brownian motion. We remark that (2.5) does not account for particle–particle interactions such as flocculation or hindered settling.

We restrict ourselves to two-dimensional systems, which allows us to replace (2.1) and (2.2) by a streamfunction–vorticity formulation of the form

$$\boldsymbol{u} = \left(\frac{\partial \psi}{\partial z}, -\frac{\partial \psi}{\partial x} \right), \tag{2.6}$$

$$\omega = \boldsymbol{\nabla} \times \boldsymbol{u}, \tag{2.7}$$

$$\omega = -\nabla^2 \psi, \tag{2.8}$$

$$\rho_0 \left(\frac{\partial \omega}{\partial t} + \boldsymbol{u} \cdot \boldsymbol{\nabla} \omega \right) = \mu \nabla^2 \omega - \frac{\partial \rho}{\partial x} g. \tag{2.9}$$

The choice of characteristic quantities is complicated by the fact that, when dealing with an unbounded, initially stationary fluid, no length or velocity scales *initially* present themselves. As the system develops, length scales in the form of diffusive interface thicknesses and an unstable layer due to settling will develop, as will be discussed in more detail below. However, we follow the analysis of Chandrasekhar (1961) and take viscous scales for both length and time. We differ from Chandrasekhar in that we use a reduced gravity, defined as $g' = (\Delta\rho/\rho_0)g = \gamma C_{max} g$. Here we have chosen our characteristic density difference to be the difference in the particle loading because in all of our scenarios this will represent the magnitude of the density difference at the unstable interface. The characteristic quantities thus take the forms:

$$L^c = \left(\frac{\nu^2}{g'} \right)^{1/3}, \tag{2.10}$$

$$T^c = \left(\frac{\nu}{g'^2} \right)^{1/3}, \tag{2.11}$$

$$U^c = (\nu g')^{1/3}, \tag{2.12}$$

$$P^c = \rho_0 (\nu g')^{2/3}, \tag{2.13}$$

https://doi.org/10.1017/jfm.2011.474 Published online by Cambridge University Press

$$S^c = S_{max}, \tag{2.14}$$

$$C^c = C_{max}. \tag{2.15}$$

Based on these characteristic quantities, we obtain as dimensionless parameters:

$$V_p^* = \frac{V_p}{(\nu g')^{1/3}}, \tag{2.16}$$

$$R_s^* = \frac{\alpha S_{max}}{\gamma C_{max}}, \tag{2.17}$$

$$Sc_i^* = \frac{\nu}{D_i}. \tag{2.18}$$

Here R_s^* is the stability ratio, as defined in the salt finger literature (Huppert & Manins 1973), Sc_i^* are the Schmidt numbers of the two scalars affecting the density, and αS_{max} and γC_{max} refer to the maximum added density due to salinity and particles, respectively. From this point onward all variables will be in dimensionless form unless otherwise noted, and we will drop the star notation. After applying the characteristic quantities to (2.4), (2.5), (2.8) and (2.9), we obtain:

$$\omega = -\nabla^2 \psi, \tag{2.19}$$

$$\frac{\partial \omega}{\partial t} + \boldsymbol{u} \cdot \boldsymbol{\nabla} \omega = \nabla^2 \omega - \frac{\partial}{\partial x}(R_s S + C), \tag{2.20}$$

$$\frac{\partial S}{\partial t} + \boldsymbol{u} \cdot \boldsymbol{\nabla} S = \frac{1}{Sc_s} \nabla^2 S, \tag{2.21}$$

$$\frac{\partial C}{\partial t} - V_p \frac{\partial C}{\partial z} + \boldsymbol{u} \cdot \boldsymbol{\nabla} C = \frac{1}{Sc_c} \nabla^2 C. \tag{2.22}$$

2.2. *Linearization*

The stability analysis is constructed by linearizing the above equations around a one-dimensional base state. This linearization takes the form:

$$\psi(x, z, t) = 0 + \psi'(x, z, t), \tag{2.23}$$

$$\omega(x, z, t) = 0 + \omega'(x, z, t), \tag{2.24}$$

$$S(x, z, t) = \bar{S}(z) + S'(x, z, t), \tag{2.25}$$

$$C(x, z, t) = \bar{C}(z) + C'(x, z, t). \tag{2.26}$$

The base states for both ψ and ω are taken to be zero, indicating a quiescent base state. Note that the base state is assumed to be quasi-steady, i.e. independent of time. The implications of this assumption will be discussed in detail below. We assume wave-like perturbations of the form

$$\psi'(x, z, t) = \hat{\psi}(z) \sin(kx)\, \mathrm{e}^{\sigma t}, \tag{2.27}$$

$$\omega'(x, z, t) = \hat{\omega}(z) \sin(kx)\, \mathrm{e}^{\sigma t}, \tag{2.28}$$

$$S'(x, z, t) = \hat{S}(z) \cos(kx)\, \mathrm{e}^{\sigma t}, \tag{2.29}$$

$$C'(x, z, t) = \hat{C}(z) \cos(kx)\, \mathrm{e}^{\sigma t}. \tag{2.30}$$

Upon substitution of these expressions into the governing equations, and keeping only the terms that are linear in the perturbation, we obtain a generalized eigenvalue problem of the form

$$\boldsymbol{A}\boldsymbol{x} = \sigma \boldsymbol{B}\boldsymbol{x}, \tag{2.31}$$

https://doi.org/10.1017/jfm.2011.474 Published online by Cambridge University Press

$$\boldsymbol{A} = \begin{pmatrix} \boldsymbol{M} & \boldsymbol{I} & 0 & 0 \\ 0 & \boldsymbol{M} & kR_s\boldsymbol{I} & k\boldsymbol{I} \\ k\dfrac{\mathrm{d}\bar{S}}{\mathrm{d}z}\boldsymbol{I} & 0 & \dfrac{1}{Sc_s}\boldsymbol{M} & 0 \\ k\dfrac{\mathrm{d}\bar{C}}{\mathrm{d}z}\boldsymbol{I} & 0 & 0 & \dfrac{1}{Sc_c}\boldsymbol{M} + V_p D_z \end{pmatrix}, \tag{2.32}$$

$$\boldsymbol{B} = \begin{pmatrix} 0 & 0 & 0 & 0 \\ 0 & \boldsymbol{I} & 0 & 0 \\ 0 & 0 & \boldsymbol{I} & 0 \\ 0 & 0 & 0 & \boldsymbol{I} \end{pmatrix}, \tag{2.33}$$

$$\boldsymbol{M} = -k^2\boldsymbol{I} + D_z^2. \tag{2.34}$$

Here D_z represents the derivative with respect to z, while $\boldsymbol{I}$ denotes the identity matrix. We look for bounded solutions to (2.31) where σ represents the growth rate, with a positive (negative) real part indicating an unstable (stable) configuration. A non-zero imaginary part of σ would represent an oscillatory solution, as is seen in double diffusive problems where the slower diffusing component is stably stratified (Turner 1973). However, in the course of the present study, we have found only purely real eigenvalues. The eigenfunctions are $\boldsymbol{x} = [\hat{\psi}, \hat{\omega}, \hat{S}, \hat{C}]^{\mathrm{T}}$. This problem has a large parameter space to explore, as the growth rate depends on the wavenumber k of the perturbation, on the settling speed V_p, on the Schmidt numbers Sc_i of both species, and on the stability ratio R_s. In addition, the shapes of the base concentration profiles present additional parameters.

3. Numerical method

3.1. *Rational spectral approximation*

In order to solve the above eigenvalue problem numerically, we first discretize the spatial derivatives using a rational collocation method. While rational interpolants are not a new subject (Berrut & Trefethen 2004), their use as a spectral collocation method for solving boundary value problems has received a growing amount of attention in recent years (Berrut & Mittelmann 2004; Tee & Trefethen 2006; Cueto-Felgueroso & Juanes 2009). This interest is mainly due to the ease with which the method can be adapted to different tasks. The present problem involves narrow interfacial regions requiring fine resolution, in conjunction with a domain size that needs to be sufficiently large for the perturbations to decay. Traditional equidistant finite difference methods either under-resolve the interfacial regions, resulting in a loss of accuracy, or over-resolve the regions away from the interfaces, driving up the computational cost. Stretched finite difference methods can alleviate the problem of resolution at the interface, but they still lack the efficiency of spectral methods. The use of traditional Chebyshev methods requires transforming the original differential equations into new coordinates, which adds the difficulty of finding the derivatives of the grid transformation (Tee & Trefethen 2006). Alternatively, a patched Chebyshev method could be employed by splitting the domain at the interfacial regions and applying matching conditions on the function and its normal derivative at the boundary. However, a rational spectral method is both more straightforward and easier to implement, as only the grid nodes themselves need to be transformed, while other

https://doi.org/10.1017/jfm.2011.474 Published online by Cambridge University Press

aspects of the method, such as building the derivative matrices, performing the interpolation, etc., remain unchanged.

The rational interpolant is most commonly written in the barycentric form

$$f(z) \simeq \frac{\displaystyle\sum_{k=0}^{N} \frac{w_k}{z - z_k} f_k}{\displaystyle\sum_{k=0}^{N} \frac{w_k}{z - z_k}}, \tag{3.1}$$

where w_k represents the barycentric weights, z_k denotes the grid nodes and f_k indicates the function values on the grid. The weights are generally defined as

$$w_k = \frac{1}{\displaystyle\prod_{j=0,\, j\neq k}^{N} (z_j - z_k)}. \tag{3.2}$$

However, for the special case of the Chebyshev nodes, $z_k = \cos(k\pi/N)$, the weights have the simplified definition

$$w_k = \begin{cases} \dfrac{1}{2}, & k = 0, \\ (-1)^k, & \text{else}, \\ \dfrac{1}{2}(-1)^N, & k = N. \end{cases} \tag{3.3}$$

We can also use (3.1) to find the derivatives of the interpolant. The first-order differentiation matrix is defined as

$$D^{(1)}_{i,j} = \begin{cases} \dfrac{w_j/w_i}{z_i - z_j}, & i \neq j, \\ \displaystyle -\sum_{k=0,k\neq j}^{N} D^{(1)}_{i,k}, & i = j, \end{cases} \tag{3.4}$$

and the second-order matrix as

$$D^{(2)}_{i,j} = \begin{cases} 2D^{(1)}_{i,j}\left(D^{(1)}_{i,i} - \dfrac{1}{z_i - z_j}\right), & i \neq j, \\ \displaystyle -\sum_{k=0,k\neq j}^{N} D^{(2)}_{i,k}, & i = j. \end{cases} \tag{3.5}$$

The derivative of a function at a grid location, z_i, is then computed as

$$\frac{\mathrm{d}f}{\mathrm{d}z}(z_i) = \sum_{j=0}^{N} D_{i,j} f(z_j). \tag{3.6}$$

3.2. *Implementation*

We transform the grid nodes, in order to deal with the narrow interfacial regions of the base state. The domain is truncated at a sufficiently large distance to ensure a negligible influence of the boundaries, where we apply homogeneous

https://doi.org/10.1017/jfm.2011.474 Published online by Cambridge University Press

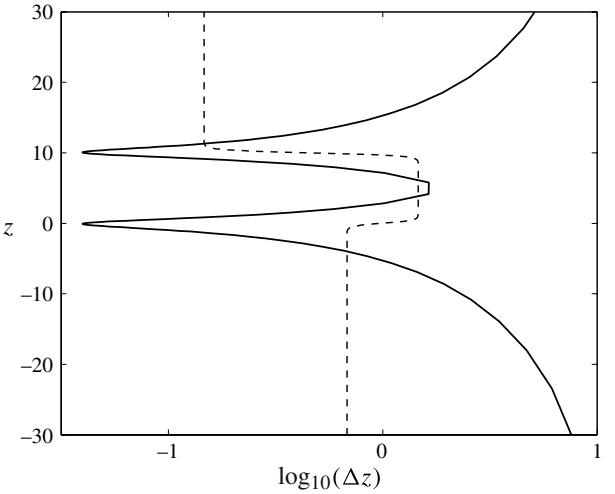


FIGURE 2. The grid spacing (solid line) and the density profile (dashed line). The transformation function provides a fine resolution of the interfacial regions, with 50 % of the grid nodes covering ∼3 % of the domain.

Dirichlet conditions. We use the grid transformation function introduced by Berrut & Mittelmann (2004) for dealing with multiple fronts:

$$y_k = g^{-1}(\bar{z}) = \eta + \frac{1}{\lambda}\sum_{q=1}^{2} \operatorname{atan}(\theta_q(\bar{z}_k - \phi_q)). \tag{3.7}$$

Here y_k represents the Chebyshev nodes, $\bar{z}_k$ the scaled physical grid nodes, θ_q and ϕ_q the steepness and location of the fronts, respectively, and η and λ are parameters that ensure that g maps $[-1, 1]$ onto itself. To determine the physical grid nodes, we reformulate (3.7) into a quadratic equation in $\bar{z}_k$ using trigonometric identities. We then scale and translate $\bar{z}_k$ to get the physical grid nodes z_k:

$$L_{top} = H + C_L\left(\frac{2\pi}{k}\right) + C_{V_p}^{top}\left(\frac{2\pi}{k}\right)(\mathrm{e}^{V_p} - 1), \tag{3.8}$$

$$L_{bot} = 0 + C_L\left(\frac{2\pi}{k}\right) + C_{V_p}^{bot}\left(\frac{2\pi}{k}\right)(\mathrm{e}^{V_p} - 1), \tag{3.9}$$

$$z_k = \bar{z}_k\left(\frac{L_{top} + L_{bot}}{2}\right) + \left(\frac{L_{top} - L_{bot}}{2}\right). \tag{3.10}$$

Here L_{top} and L_{bot} are the upper and lower extrema of the domain, while C_L, $C_{V_p}^{top}$ and $C_{V_p}^{bot}$ are constants that are chosen to ensure a negligible influence of the boundaries. Problem parameters are represented by: H, the height of the unstable layer; V_p, the settling velocity; and k, the wavenumber.

A sample grid for an unstable layer height $H = 10$ and settling velocity $V_p = 0$ is shown in figure 2. The domain extends from $z_{min} = -52.7$ to $z_{max} = 62.7$ and employs 121 grid nodes. While the median grid spacing is $\Delta z = 0.1147$, half of the grid nodes are placed in the regions $z \in [-1.1, 0.6]$ and $z \in [9.3, 11]$. In this way, the particle and salinity interfacial regions ($C, S \in [0.1, 0.9]$) are resolved by 12 nodes each. To

https://doi.org/10.1017/jfm.2011.474 Published online by Cambridge University Press

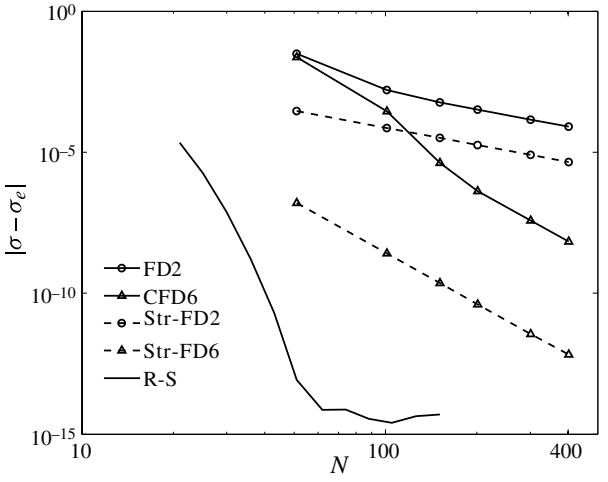


FIGURE 3. Convergence of σ with increasing N. The rational spectral method has retained spectral accuracy after applying the grid transformation. It also obtains much higher accuracy for any given grid size than any of the four finite difference methods tested. Here σ_e is taken to be the R-S solution with $N = 201$.

accomplish this resolution with an equidistant finite difference grid would require $\Delta z = 0.073$ and $N = 1568$.

The singularity of the $\boldsymbol{B}$ matrix can lead to slower convergence of the eigenvalue solvers. Thus we employ the approach of Graf, Meiburg & Härtel (2002) and modify the streamfunction equation by adding a small term to it, resulting in

$$\sigma\hat{\psi} = Re_{num}[\hat{\omega} + (-k^2 + D^2)\hat{\psi}]. \tag{3.11}$$

We choose Re_{num} such that we do not modify the eigenvalues by more than 0.01 %. This numerical modification reduces the $\boldsymbol{B}$ matrix to the identity matrix. The eigenvalue problem is subsequently solved by means of the MATLAB routine `eig`.

3.3. *Convergence*

In the previous section, we summarized our motivation for using the rational spectral method over more traditional methods. In figure 3, we compare the convergence of five different methods: second-order uniform finite differences (FD2), sixth-order uniform compact finite differences (CFD6) (Lele 1992), second-order stretched finite difference (Str-FD2), sixth-order stretched finite differences (Str-FD6), and the rational spectral collocation method (R-S). The rational spectral method produces significantly higher accuracy for a given number of grid points than any of the finite difference methods. More practically, the rational spectral method can achieve a full 15 digits of accuracy with less CPU time than it took any of the finite difference methods to find a solution on their coarsest grid. It should be noted that, for large values of N, the finite difference methods were solved using the MATLAB sparse eigenvalue solver, `eigs`, because it uses an iterative method to find only a fraction of all possible eigenvalues and thus performed much faster than `eig` for large N. The rational spectral method was always solved using `eig`.

We performed various convergence tests to optimize the accuracy of the numerical method. The parameters we optimized were: C_L, a domain constant; θ, the grid clustering; and Re_{num}, the artificial term in the Poisson equation. For these parameters,

https://doi.org/10.1017/jfm.2011.474 Published online by Cambridge University Press

we used the convergence of both eigenvalues and eigenvectors as an indicator of accuracy.

When determining the domain constant C_L, we use the wavelength of the perturbation as a starting point. In the simplest case of one scalar component and no settling velocity, the domain extends a multiple of this wavelength in both directions, $L_{top} = L_{bot} = C_L(2\pi/k)$. Figure 4 shows the results of our investigation for three different criteria. The first two criteria look at the behaviour of the eigenfunctions at the boundaries, where we enforce a value of zero. However, enforcing this condition is not enough to ensure that the boundaries do not influence the eigenfunctions. Consequently, we examine both the eigenfunction value one point away from the boundary $\hat{\psi}_{L_{top}-1}$, as well as the eigenfunction derivative $\hat{\psi}_{L_{top'}}$ at the boundary itself. Both of these values should tend to zero if the domain is appropriately large, and the figure shows that they do. The other criterion is the convergence of the eigenvalues themselves. While a computational domain size of three wavelengths shows sufficient convergence of the eigenvalues, adding an additional wavelength to the domain size provides much better convergence in the eigenvectors. Hence, we chose four wavelengths for our calculations. Any additional increases in the size of the domain, for a constant number of grid points, would only decrease the resolution at the interfacial regions.

The importance of the numerical parameter, Re_{num}, introduced in (3.11) is to speed up the eigenvalue solver without modifying the eigenvalues. Thus, the terms on the right-hand side need to be much larger than the term on the left-hand side. Rearranging the equation, this tells us that the value of $\sigma\hat{\psi}/Re_{num}$ needs to be sufficiently small. We found that a value of $Re_{num} = 10^4$ does not modify the eigenvalues by more than 0.01 %.

3.4. *Validation*

To validate the eigenvalue solver, we focus on the problem analysed by Batchelor & Nitsche (1991). The eigenvalues we obtain for the base state

$$\bar{C}(z) = 0.5\,\mathrm{erf}\left(\frac{z}{L}\right) \tag{3.12}$$

agree with those given in their figure 8(*a*), to within the resolution of the figure.

4. Settling particles only

4.1. *Analytical results for step profiles*

The classic Rayleigh–Taylor instability is a well-studied problem. Notably, Chandrasekhar (1961) examined the stability of a step density profile in the absence of mass diffusion. Here, we extend his analysis to include the effect of a constant settling velocity for the scalar concentration field, in the absence of diffusion, as a model of a particulate phase. We focus on the case where only particles contribute to the density of the fluid, with the particle concentration base state taken as

$$\bar{C}(z) = \begin{cases} 1, & z > 0, \\ 0, & z < 0. \end{cases} \tag{4.1}$$

In order to obtain a steady base state, we shift to a reference frame that moves downwards with the particles. Thus, the base state now has a constant upward fluid velocity that is equal in magnitude and opposite in sign to the settling velocity of the

https://doi.org/10.1017/jfm.2011.474 Published online by Cambridge University Press

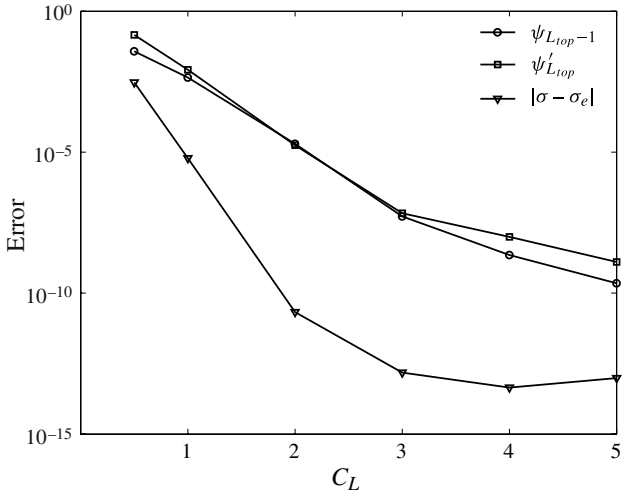


FIGURE 4. Three different error measures for determining the optimal domain height, where C_L represents the domain half-height measured in perturbation wavelengths. The domain needs to be sufficiently large so as to allow the eigenfunctions to decay to zero, without being so large as to reduce the resolution of the method.

particles. By combining the equations for the streamfunction, vorticity and particles for the modified base state, we arrive at the governing equation

$$(-k^2 + D_z^2)(\sigma + V_p D_z - (-k^2 + D_z^2))\hat{\psi} = \frac{-k^2}{\sigma}\frac{\mathrm{d}\bar{C}(z)}{\mathrm{d}z}\hat{\psi}. \tag{4.2}$$

Owing to the choice of a step profile, the right-hand side of (4.2) vanishes away from the interface, so that we can express $\hat{\psi}$ as a linear combination of the two roots of the governing equation

$$\hat{\psi}(z) = A\,\mathrm{e}^{\pm kz} + B\,\mathrm{e}^{\pm qz}, \tag{4.3}$$

$$\pm q = \frac{V_p}{2} \pm \sqrt{\left(\frac{V_p}{2}\right)^2 + k^2 + \sigma}. \tag{4.4}$$

The boundary conditions are enforced by admitting only those exponential functions that decay to zero far from the interface. We can then solve for the growth rate, σ, and the coefficients of $\hat{\psi}$ by applying matching conditions at the interface. These conditions are

$$\Delta_i(\hat{\psi}) = 0, \tag{4.5}$$

$$\Delta_i(D\hat{\psi}) = 0, \tag{4.6}$$

$$\Delta_i(D^2\hat{\psi}) = 0, \tag{4.7}$$

$$\Delta_i(D^3\hat{\psi}) = \frac{k^2}{\sigma}\Delta_i(\bar{C})\hat{\psi}_i. \tag{4.8}$$

Here $\Delta_i(f) = f(i^+) - f(i^-)$ denotes the jump in the quantity f across the interface. Equation (4.5) represents the continuity of the vertical velocity component, and (4.6) the continuity of the horizontal velocity component as derived from the continuity equation. Equation (4.7) indicates the continuity of shear stress at the interface,

https://doi.org/10.1017/jfm.2011.474 Published online by Cambridge University Press

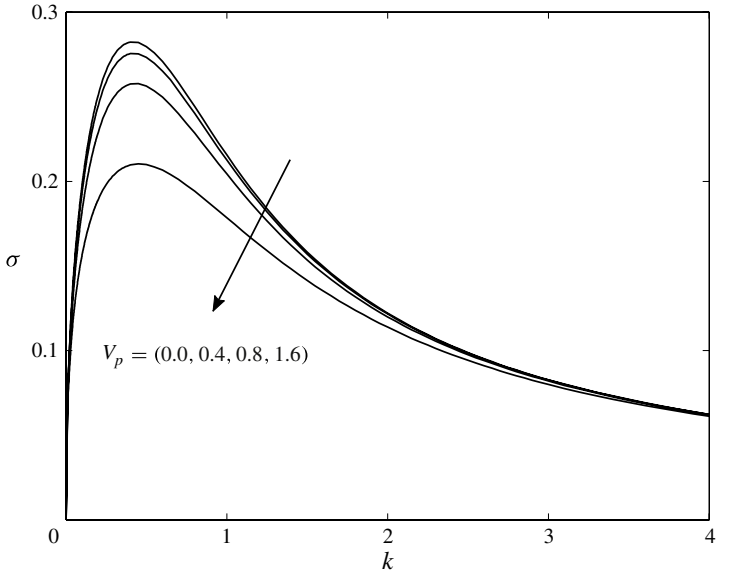


FIGURE 5. Dispersion curves for step-like particle concentration profiles settling through constant-density fluid. With increasing settling velocity, the growth rate decreases. The long- to moderate-wavelength perturbations are most strongly affected by changes in the settling velocity.

and (4.8) the jump in the derivative of pressure across the interface caused by the concentration base state, as derived from the momentum equations. Using these matching conditions, we obtain a nonlinear equation for the growth rate σ, with dependence on the wavenumber k and the settling velocity V_p.

An immediate result is seen in the fact that the characteristic root q has two different values in the upper and lower layers. The modulus of q is lower in the upper region, indicating that the perturbation decays more slowly there. Physically, this signifies that the vorticity generated by baroclinic effects at the density jump, in addition to diffusing, also has a tendency to remain attached to the fluid elements as the particles settle through the fluid. Hence, the vorticity is effectively convected away from the interface in the upper fluid layer, so that its profile is smoothed out. Conversely, in the lower fluid layer, the vorticity profile steepens, as the fluid particles move towards the interface. This affects the shape of the eigenmodes as well as the growth rate. Figure 5 shows dispersion curves for increasing settling velocities. As the settling velocity is increased, it is evident that the growth rate decreases, which follows from the smearing of the vorticity in the interfacial region. Figure 6 demonstrates the smearing effect in more detail, within a region extending one wavelength above and below the interface.

Figure 7(*a*) shows how the growth rate is affected by particle settling, for different wavenumbers. We find that small settling velocities have a vanishing effect, whereas larger settling velocities lead to a power-law decay of the growth rate. For the most unstable wavenumber k_{max}, the transition between these regions occurs near $V_p = 1$. Here the physical settling velocity of the particles is equal to the viscous velocity scale U^c, which characterizes the fluid velocity of the instability and is defined as the ratio of L^c, a measure of the dominant wavelength of the instability, to T^c, the time scale associated with amplitude doubling. When $V_p \ll 1$, the instability develops much faster

https://doi.org/10.1017/jfm.2011.474 Published online by Cambridge University Press

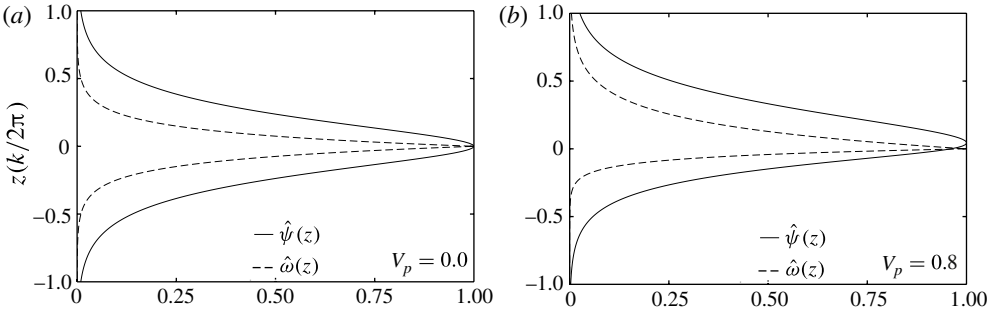


FIGURE 6. The loss of symmetry in the $\hat{\psi}$ and $\hat{\omega}$ eigenmodes as a result of particle settling velocity: (*a*) vanishing settling velocity; (*b*) finite settling velocity. The solid line represents the streamfunction, $\hat{\psi}$, while the dashed line indicates the vorticity, $\hat{\omega}$. For finite settling velocities, the vorticity exhibits a strong steepening for $z < 0$, and a smearing for $z > 0$.

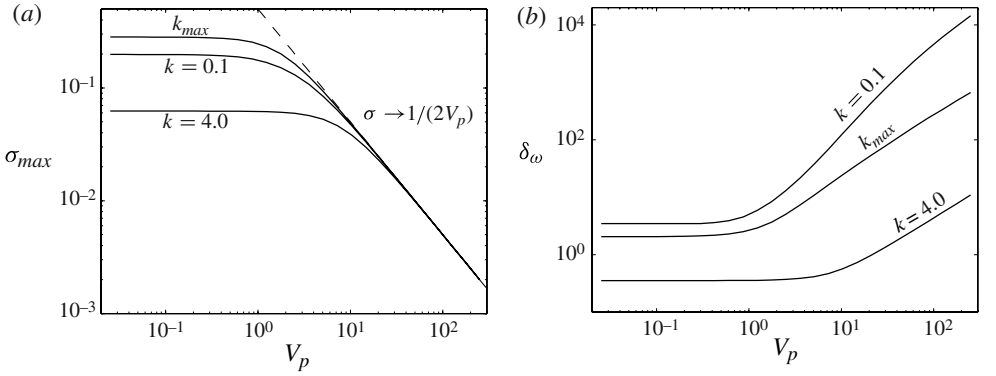


FIGURE 7. (*a*) The maximum growth rate is unaffected by very small V_p, but shows a power-law decay for large settling velocities. (*b*) The 'smearing' of the vorticity can be quantified by the width of the $\omega = 0.5$ layer. A strong correlation is observed between the amount of 'smearing' experienced by the vorticity field and the reduction in the growth rate.

than the particle front moves, so that the settling velocity has very little effect on the growth. However, when $V_p \gg 1$, the particle front moves faster than the instability develops, and hence the growth of the instability is reduced. In the limit of very high settling velocities, the dispersion relationship loses all dependence on k and approaches the limiting value of $0.5V_p^{-1}$. This suggests that, for large settling velocities, the more appropriate time scale of the problem is $V_p g'^{-1}$, which is no longer a viscous time scale. It should be noted that the most unstable wavenumber has a weak dependence on the settling velocity.

The thin layer of vorticity near the density jump represents the main length scale in this system, which was initially devoid of one. The thickness of this vorticity layer is governed by the balance of viscous diffusion and convection due to particle settling. We quantify this layer by the distance δ_ω between the two locations where the vorticity eigenfunction has half of its maximum value,

$$\delta_\omega = z(z > 0, \hat{\omega} = 0.5) - z(z < 0, \hat{\omega} = 0.5). \tag{4.9}$$

https://doi.org/10.1017/jfm.2011.474 Published online by Cambridge University Press

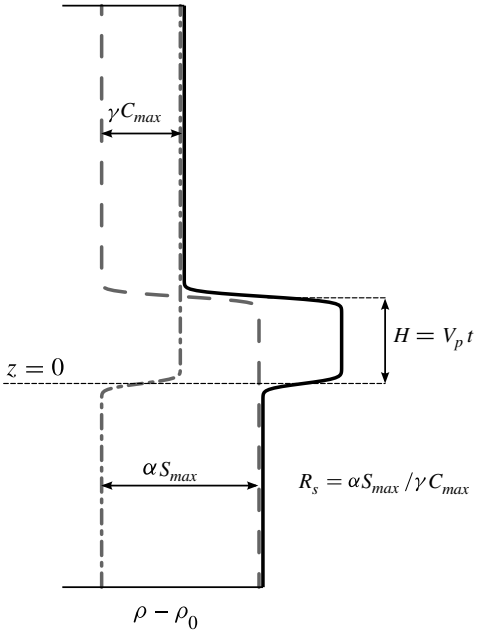


FIGURE 8. Sketch of the base state density profile in a salinity–particle system. The parameters α and γ are dimensionless numbers that quantify the maximum density loading due to salinity and particles, respectively. The thickness of the unstable layer is indicated by H. The stability ratio R_s represents the ratio of the added densities of salinity and particles, respectively. In the moving reference frame, the location of the particle interface is defined as $z = 0$.

Figure 7(*b*) shows the width of the vorticity layer, δ_ω. We observe a strong correlation between the onset of smearing and the decay of the growth rate.

5. Multi-component systems

The analysis of the previous section allowed us to isolate the effect of a settling velocity on the growth of gravitational instabilities. However, density profiles more relevant to oceanic applications include the additional influence of salinity and temperature. To address more realistic conditions, we now focus on base states of the type shown in figure 8. This type of profile arises, for example, in the case of a salt wedge estuary, such as the South Pass of the Mississippi Delta. Wright & Coleman (1974) noted that, in South Pass, suspended sediment loading is highest in the freshwater layer and achieves a maximum at the density interface. The authors noted that some of the sediment that they expected to be transported as bed-load is carried much further downstream in suspension. Another example of such a density distribution can be found in intermontane lakes. Pharo & Carmack (1979) observed such a lake and measured the highest suspended sediment concentration above the thermocline, with a conspicuous absence of turbidity in the lake water below. In the absence of salt, this lake is stratified due to heating of the upper layer, which creates a similar profile as figure 8, with temperature playing the role of salinity.

Returning to figure 8, even if all species diffusion coefficients (particles and salinity or temperature) were identical, these can develop gravitational instabilities of Rayleigh–Taylor (RT) type. Our interest will focus on how these purely gravitational

https://doi.org/10.1017/jfm.2011.474 Published online by Cambridge University Press

effects are modified by double diffusive (DD) effects due to differences in the diffusion coefficients. We note that it is no longer possible to obtain a steady base state by shifting to a reference frame moving with the particle front, as the unstable layer thickness $H = V_p t$ depends on time. Nevertheless, since we expect instabilities to develop preferentially around the gravitationally unstable lower boundary of the unstable layer, we continue to employ the reference frame moving with the particles. When conducting a formal linear stability analysis, we will generally make the quasi-steady-state assumption (QSSA), i.e. we will assume that the time scale associated with the growth of the instability is much faster than the time scale of any base state changes, *viz.* the diffusive growth of the salinity interface and the convective growth of the unstable layer thickness. Strictly speaking, the range of validity of the QSSA can be checked only *a posteriori*, by means of fully nonlinear simulations. Before proceeding to a formal linear stability analysis, we will investigate the stability limit of time-dependent base state profiles.

5.1. *Analytical results*

The addition of a second diffusive component (salinity or temperature) contributing to the density, in addition to particles, means that double diffusive fingering instabilities are now possible. This is especially true as particles diffuse orders of magnitude more slowly than both salinity and temperature. As in the previous section, the starting point for our analysis will be vertical base state profiles in the reference frame moving with the particle front, which we now take to be of the form

$$\bar{C}(z,t) = 0.5 + 0.5\,\mathrm{erf}\left(\frac{z}{l_c(t)}\right), \tag{5.1}$$

$$\bar{S}(z,t) = 0.5 - 0.5\,\mathrm{erf}\left(\frac{z - V_p t}{l_s(t)}\right), \tag{5.2}$$

$$l_i(t) = \left(\frac{4t}{Sc_i}\right)^{1/2}, \tag{5.3}$$

where we assume that at time $t = 0$ the fronts are sharp, and subsequently diffuse. Huppert & Manins (1973) considered corresponding profiles, without settling, to analyse the situation of hot, salty water above colder, fresher water. They employed the known result for the onset of double diffusion in a linearly stratified system, which for our system of sediment-laden, fresh water above clear, salty water states that the system is unstable when

$$-R_s \frac{\mathrm{d}\bar{S}/\mathrm{d}z}{\mathrm{d}\bar{C}/\mathrm{d}z} < \left(\frac{Sc_c}{Sc_s}\right) = \left(\frac{D_s}{D_c}\right) = \tau. \tag{5.4}$$

Huppert & Manins (1973) assume that instability will occur when this criterion is first exceeded at any z location. For diffusing, error function-type base states, they find that the minimum value of the left-hand side occurs at $z = 0$ for all times, and that it scales with $\tau^{-1/2}$. Hence, the condition for instability becomes $R_s < \tau^{3/2}$.

We can now extend this analysis to non-zero settling velocities. By substituting the base states (5.1)–(5.3) into (5.4), we obtain

$$R_s \left(\frac{l_c}{l_s}\right) \exp\left[-\frac{(z - V_p t)^2}{l_s^2} + \frac{z^2}{l_c^2}\right] < \tau. \tag{5.5}$$

https://doi.org/10.1017/jfm.2011.474 Published online by Cambridge University Press

Here, the minimum value of the exponential occurs at $z = -V_p t\,(\tau - 1)^{-1}$. However, for the large values of τ typical for particle–salinity (or particle–temperature) systems, this value is close to zero, at least for short times, so that the instability criterion becomes

$$R_s < \tau^{3/2} \exp\left[R_t^2\right], \tag{5.6}$$

$$R_t = \frac{V_p t}{\sqrt{4t/Sc_s}}. \tag{5.7}$$

We note the introduction of the dimensionless thickness ratio R_t, which compares the unstable layer thickness to the salinity interface thickness. Its influence will be discussed in more detail below. The first expression tells us a few important features about double diffusive fingering in a settling system. First, in the limit of $V_p = 0$, we recover the original result of Huppert & Manins (1973). Secondly, the instability is most dangerous near the particle interface $z \approx 0$, and not at the stable salinity interface. In fact, (5.5) evaluated at the particle interface $z = 0$ shows that the threshold below which instability occurs increases with time (indicating that the system becomes more unstable there), while at the stable interface $z = V_p t$ this threshold value decreases and the system becomes more stable. Equation (5.6) furthermore shows that, for any $R_t > 0$, the instability threshold is increased at the particle interface. In fact, the more rapidly the particles settle compared to the diffusive spreading of the salinity, the greater the threshold value becomes. The question of how the gravitational instability of the particle interface is modulated by double diffusive effects will be addressed below.

This analysis can be generalized to profiles with a non-zero initial interface thickness, as noted by Huppert & Manins (1973, footnote on p. 319). In a typical river outflow environment, mixing due to turbulence or other phenomena will create a well-mixed region in the area of the interface, rather than an initial step profile. The addition of an initial interface thickness l_0 modifies (5.3) to

$$l_i(t) = \left(\frac{4t}{Sc_i} + l_0^2\right)^{1/2}. \tag{5.8}$$

It is furthermore useful to define a quantity, $\hat{\tau}$, that represents the time-dependent ratio of the interface thicknesses,

$$\hat{\tau}(t) = \left(\frac{l_s(t)}{l_c(t)}\right)^2 = \tau \left(\frac{t + 0.25\, l_0^2\, Sc_s}{t + 0.25\, l_0^2\, Sc_c}\right). \tag{5.9}$$

Initially, the two interfaces have the same width and thus $\hat{\tau}(0) = 1$. However, for long times, diffusive spreading will result in $\hat{\tau}(\infty) \to \tau$. With these definitions, the criterion for instability becomes

$$R_s < \tau\hat{\tau}\,(t)^{1/2} \exp\left[R_t^2 \left(\frac{\hat{\tau}}{\hat{\tau} - 1}\right)\left(1 + 0.25\, l_0^2\, Sc_s\, t^{-1}\right)^{-1}\right]. \tag{5.10}$$

Interestingly, at early times $t \approx 0$, the right-hand side now scales linearly with τ, rather than with $\tau^{3/2}$. During these early times, the large values of τ typical for particle–salinity systems thus can substantially reduce the value of R_s below which instability will occur, thereby rendering the system more stable. The above expression for $\hat{\tau}$ allows us to estimate the time after which the finite initial layer thickness will no longer influence the stability behaviour. For this to occur, $\hat{\tau}$ needs to scale as τ, which

https://doi.org/10.1017/jfm.2011.474 Published online by Cambridge University Press

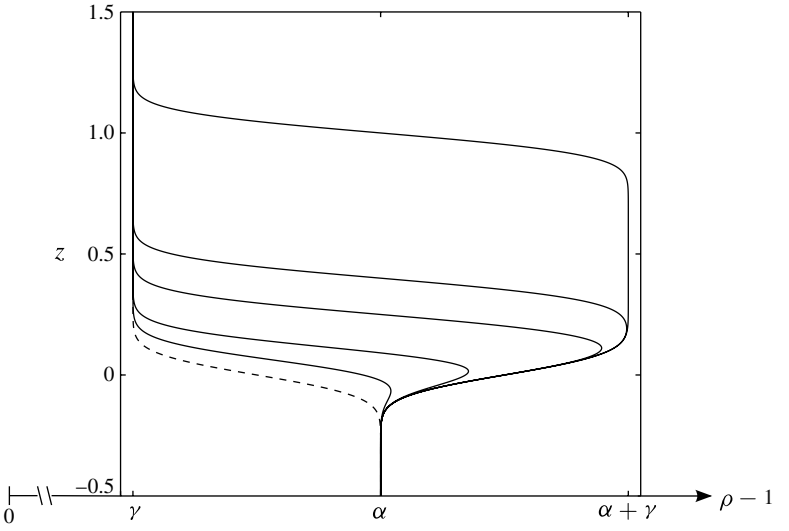


FIGURE 9. The excess density, $(\rho - 1) = \gamma C + \alpha S$, of the base state is shown for six different values of the unstable layer thickness, $H = (0, 0.04, 0.10, 0.25, 0.4, 1.0)$. The concentration and salinity profiles are defined by (5.1) and (5.2). The dotted line represents the $H = 0$ profile. The interface thicknesses are set to a constant value of $l_s = l_c = 0.1$.

requires $t = O(l_0^2 Sc_c)$. Owing to the typically large value of Sc_c, the required time is quite long, so that it is likely that the unstable layer will have grown to a significant size before then. For all but the smallest settling velocities, this means that the particle interface will be in a region of uniform salinity concentration, so that double diffusive effects will no longer be important. Therefore, in situations like these it is important to account for the initial mixed thickness.

5.2. *Model base states*

5.2.1. *Influence of the unstable layer thickness, H*

In order to analyse the modification of gravitational instabilities for $\tau = 1$ by double diffusive effects for different unstable layer heights and initial interface thicknesses, we will now focus on two families of model base states. We will begin by discussing results for the profiles in figure 9, in order to gain insight into the influence of the unstable layer thickness, H. These profiles represent the added mass due to both particles and salinity. While the particles contribute γ to the dimensionless excess density and are located above $z = 0$, the salinity contributes α and is located below $z = H$. As a first step, we set $l_s = l_c = 0.1$, $V_p = 0$ and $Sc_c = 10^6$. We remark that we will usually keep l_c at this small value, owing to the small sediment diffusion coefficient. The effect of varying l_s will be discussed below, along with the influence of a finite settling velocity.

We note that the dimensionless interface thicknesses and unstable layer height can, in principle, be cast into the form of Rayleigh numbers. As such, one might expect the system to be more unstable for larger values of the interface thickness, i.e. for larger Rayleigh numbers. However, this is not the case, as our time scale, $(\nu/g'^2)^{1/3}$, differs from the traditional time scale of l^2/ν. Thus, for our scaling it is the smallest interface thickness that exhibits the largest growth rate. We choose the value of $l_c = l_s = 0.1$ because it yields a large growth rate without being too small to resolve numerically.

https://doi.org/10.1017/jfm.2011.474 Published online by Cambridge University Press

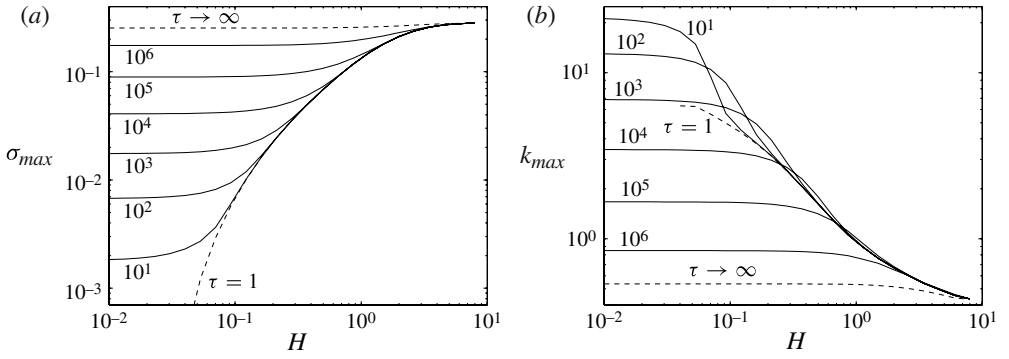


FIGURE 10. (*a*) Growth rate and (*b*) most amplified wavenumber as functions of the unstable layer height H, for different ratios τ of the diffusion coefficients. Double diffusive effects destabilize systems with thin unstable layers, when the interfaces overlap, but become negligible for thick unstable layers. Results for $l_s = l_c = 0.1$, $V_p = 0$, $Sc_c = 10^6$ and $R_s = 2$.

We expect that double diffusive effects will be most influential for small values of H, when the interfaces overlap. For larger values of the unstable layer thickness, when the interfaces become increasingly separated, we expect double diffusive effects to diminish. This is confirmed by figure 10(*a*), which shows the growth rate as a function of the unstable layer height H, for different values of τ. Thin unstable layers, which are stable for $\tau = 1$, are destabilized by double diffusive effects. We furthermore see that, for small values of H, the growth rate is independent of the unstable layer thickness. At what point the influence of the unstable layer thickness becomes noticeable depends strongly on τ. As the unstable layer thickness increases, the influence of τ becomes less and less important. For very thick unstable layers, the growth rate also becomes independent of H, as the stable salinity interface no longer influences the unstable particle interface.

Figure 10(*b*) shows that, for thin unstable layers, double diffusive effects also have a strong influence on the most unstable wavenumber. Just as for the growth rate, the dominant wavenumber depends only on τ for thin unstable layers. For thicker unstable layers, the influence of τ diminishes. For $\tau = 1$, a critical unstable layer thickness has to be exceeded for an instability to occur. Interestingly, as the value of τ increases above unity, the dominant wavelength first decreases, and then increases.

We remark that the two graphs in figure 10 also provide us with limiting information for the two instability types that we are investigating. For large values of H, the curves indicate the limiting scales for a Rayleigh–Taylor instability. For this case, our results match up well with those of Chandrasekhar (1961). While at high values of H the curves are independent of the diffusivity ratio τ, at low values of H the curves strongly depend on this parameter. This region represents the purely double diffusive finger regime. Most of the work to date on the length scales and growth rates of double diffusive fingers has addressed linearly stratified environments. However, several authors have applied results from linear gradients to the small interfacial region in the sharp gradient or 'reservoir' problem. Schmitt (1979) used such an approach and found success in matching his model to experimental data. Radko & Stern (2000) used a rigid lid model to compute flux laws numerically for fingers in 'reservoirs', and how these fluxes depend on the growth of the interfacial height. More recent numerical work by Sreenivas, Singh & Srinivasan (2009) models the entire reservoir, not just the

https://doi.org/10.1017/jfm.2011.474 Published online by Cambridge University Press

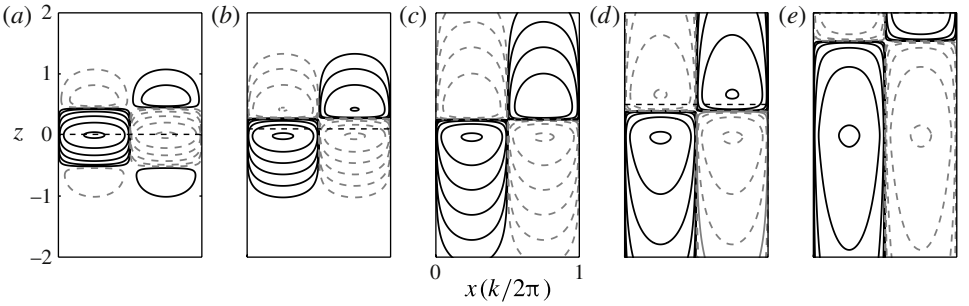


FIGURE 11. Vorticity eigenfunctions for (*a*)–(*e*) $H = (0.01, 0.10, 0.25, 0.50, 2.00)$ respectively with $k_{max} \approx (6.9, 6.0, 3.3, 1.6, 0.7)$; $\tau = 10^3$, $l_s = l_c = 0.1$, $V_p = 0$, $Sc_c = 10^6$ and $R_s = 2$. The contour values are plotted with a logarithmic scale between 0.001 and 0.9. The dashed horizontal line represents the location of the salinity interface. As the unstable layer thickness H increases, the dominant dipole structure changes to a quadrupole. For thick unstable layers, the eigenfunction at the lower interface approaches the classical Rayleigh–Taylor shape.

interface. These authors have found that finger widths scale with the Rayleigh number to the power 1/3. Our results for small H match up favourably with the results of Sreenivas *et al.* (2009), as will be discussed in more detail below.

The vorticity eigenfunctions shown in figure 11 provide insight into the changes in the instability mechanism as the influence of double diffusion diminishes. For thin unstable layers, the vorticity has a main row of dipole vortices of small vertical extent that are nearly symmetrical about the interface. However, there are also an upper and lower row of vortices with a very small magnitude, which are representative of the double diffusive character of the instability for thin unstable layers H. As H increases and the interfaces become more separated, the upper dipole of opposite sign becomes stronger, so that the overall structure takes on the shape of a quadrupole. For very thick unstable layers, the salinity interface loses its influence on the particle interface, and the dipole at the particle interface approaches the characteristic shape of the classical Rayleigh–Taylor instability.

Figure 12 analyses the role of the stability ratio R_s $(= \alpha S_{max}/\gamma C_{max})$ on the most unstable disturbances. When interpreting this figure, we need to keep in mind that length, time and velocity were made dimensionless by employing g', which in turn was based on the density difference due to particle loading. Hence it is no surprise that larger values of R_s, i.e. a larger stabilizing salinity density difference, generally result in lower growth rates. This effect is most pronounced for thin unstable layers, when the salinity and particle interfaces overlap. For large values of H, the stable salinity interface loses its influence on the unstable particle interface, so that the growth rate becomes independent of R_s. The transitional unstable layer thickness at which double diffusive effects lose their influence is largely independent of R_s.

Larger values of R_s also lead to shorter dominant wavelengths. The effects at $H \ll 1$ will be discussed in more depth in the next section. For $R_s = 1$, double diffusive effects lose their influence especially rapidly as H exceeds the thickness of the interfaces. Here we have to keep in mind that the densities above and below the unstable layer are identical, so that the overall density profile is no longer stable. For large values of H, the most unstable wavelength becomes independent of R_s, as the stable salinity interface no longer affects the instability growth at the unstable particle interface.

https://doi.org/10.1017/jfm.2011.474 Published online by Cambridge University Press

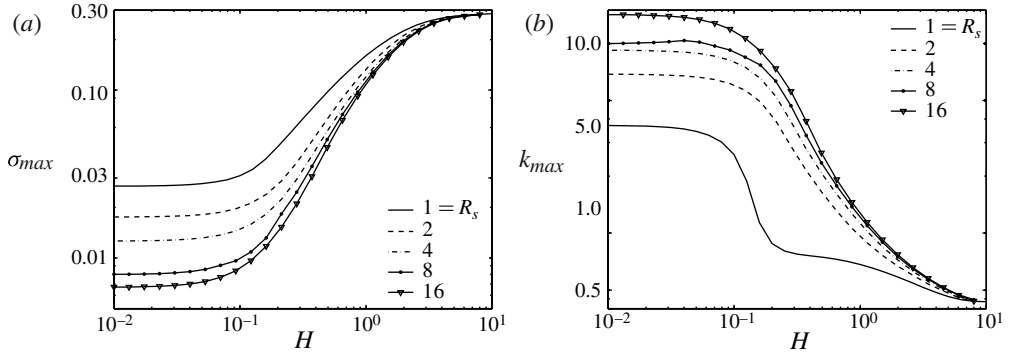


FIGURE 12. (*a*) Growth rate and (*b*) most unstable wavenumber as a function of the unstable layer thickness, for different values of the stability ratio R_s. Larger stability ratios generally result in lower growth rates and higher wavenumbers. This effect is most pronounced for thin unstable layers, when double diffusive effects are important. For thicker unstable layers, the results become independent of R_s. Results for $\tau = 10^3$, $Sc_c = 10^6$, $l_s = l_c = 0.1$ and $V_p = 0$.

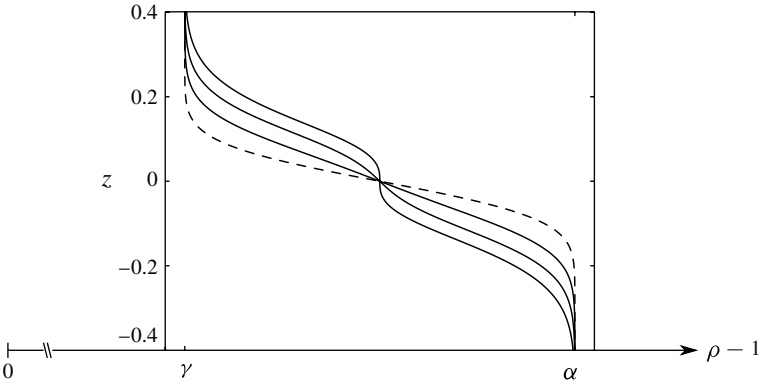


FIGURE 13. The excess density, $(\rho - 1) = \gamma C + \alpha S$, of the base state is shown for four different values of the salinity interface thickness. The concentration and salinity profiles are defined by (5.1) and (5.2) with $H = 0$. The dotted lines represent the profile for $l_s = l_c$. The final profile represents a completely flat density profile at $z = 0$, which occurs for $l_s = R_s l_c$.

5.2.2. *Salinity interface thickness l_s*

We now focus on the early-phase configuration in which there is no unstable layer yet. This allows us to analyse the influence of the salinity interface thickness l_s and the diffusivity ratio τ in isolation. For this purpose, we will focus on the set of parameters $l_c = 0.1$, $Sc_c = 10^6$, $R_s = 2$ and $V_p = 0$. The shape of the base states is depicted in figure 13. While the quasi-steady-state assumption is employed for the base state, the perturbations are of course subject to diffusion.

Figure 14 shows the maximum growth rate and the corresponding most unstable wavenumber as a function of the salinity interface thickness l_s and the diffusivity ratio τ. We remark that the z derivative of the base density profile first vanishes at $z = 0$ for $R_s = (l_s/l_c)$. For the present values of $l_c = 0.1$ and $R_s = 2$, this implies a critical salinity interface thickness of $l_s = 0.2$, so that for $\tau = 1$ an instability cannot develop below $l_s < 0.2$. However, as τ is increased above unity, we find that thinner

https://doi.org/10.1017/jfm.2011.474 Published online by Cambridge University Press

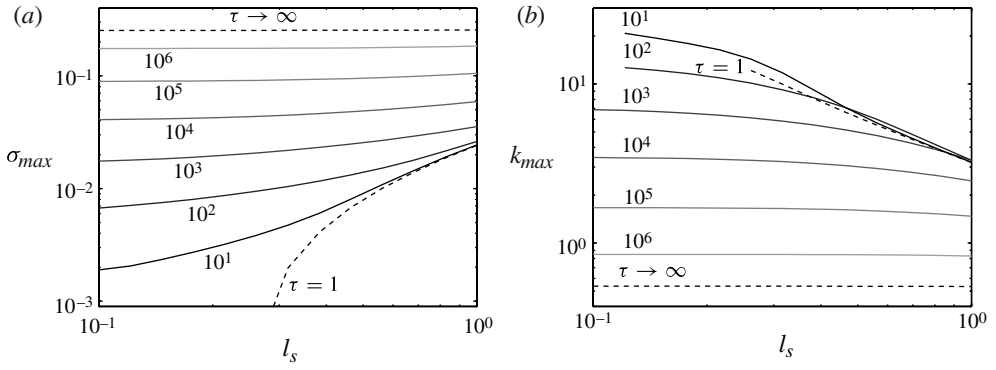


FIGURE 14. (*a*) Maximum growth rate and (*b*) corresponding most unstable wavenumber as functions of the salinity interface thickness l_s and the diffusivity ratio τ, during the initial phase when an unstable layer has not yet formed. Results for $l_c = 0.1$, $Sc_c = 10^6$, $R_s = 2$ and $V_p = 0$.

salinity interfaces quickly become unstable due to double diffusive effects. As the diffusivity ratio increases, the growth rate varies less strongly with l_s. For values of $l_s > 0.2$, the influence of τ on the growth rate quickly diminishes, as the dominant instability mode is driven more by the unstable base profile than by double diffusive effects.

For small salinity interface thicknesses dominated by double diffusive effects, we note that larger diffusivity ratios τ, i.e. larger salinity diffusion coefficients D_s, destabilize longer wavelengths. Physically, this dependence on the diffusivity ratio represents the balance between salinity diffusion driving the instability, $D_s\nabla^2 s$, and viscous forces damping it, $\nu\nabla^2\omega$. The salinity diffusion terms are composed of the diffusion coefficient D_s, and the curvature of the perturbation, which scales as k^2. Hence smaller diffusion coefficients D_s require larger curvature to overcome the viscous damping, as seen in figure 14(*b*). However, larger curvatures also result in more viscous damping of the instability, thereby leading to the smaller growth rates shown in figure 14(*a*).

Figure 15 examines the influence of the stability ratio, R_s, on the characteristics of the dominant perturbation. Here we have scaled the salinity interface thickness l_s by the stability ratio R_s. We remark that the ratio l_s/R_s effectively indicates the inverse of the stabilizing salinity gradient. This scaling results in a complete collapse of the $\tau = 1$ curves for different R_s values, and a near-collapse of the curves for $\tau > 1$. This demonstrates that it is primarily the salinity *gradient* at the interface that matters, and not so much the endpoints of the base salinity profile. Increasing salinity gradients are seen to reduce the growth rate, and increase the wavenumber of the most amplified perturbation, consistent with the curvature argument given above.

Figure 16 shows the one-dimensional eigenmodes for the density, salinity and particle fields as well as the full two-dimensional eigenmodes for density and vorticity. The calculations are for $\tau = 10^3$, $R_s = 2.0$ and $l_s = 0.2$. The value $l_s = 0.2$ was chosen because it represents the thickness at which the density base state has zero gradient at $z = 0$, the thickness before overturning occurs. However, comparisons with smaller values of l_s reveal no significant change in both of the eigenmodes, such that figure 16 can be taken as the standard mode for all calculations in this section. The vorticity mode is similar to the classical RT one with two main rolls centred about

https://doi.org/10.1017/jfm.2011.474 Published online by Cambridge University Press

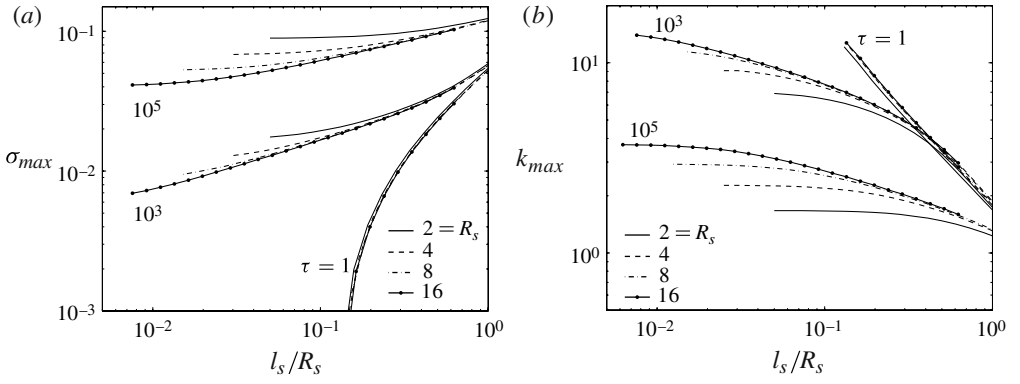


FIGURE 15. (*a*) Maximum growth rate and (*b*) corresponding most unstable wavenumber for four different values of the stability ratio, $R_s = (2,\ 4,\ 8,\ 16)$. The horizontal axis has been scaled to represent the inverse of the maximum gradient in the salinity base state. As the particle base state is fixed, this scaling results in a perfect collapse of the $\tau = 1$ curve as well as scaling of all other values of τ (values of 10^3 and 10^5 shown in figure). Calculations with $Sc_c = 10^6$ and $l_c = 0.1$.

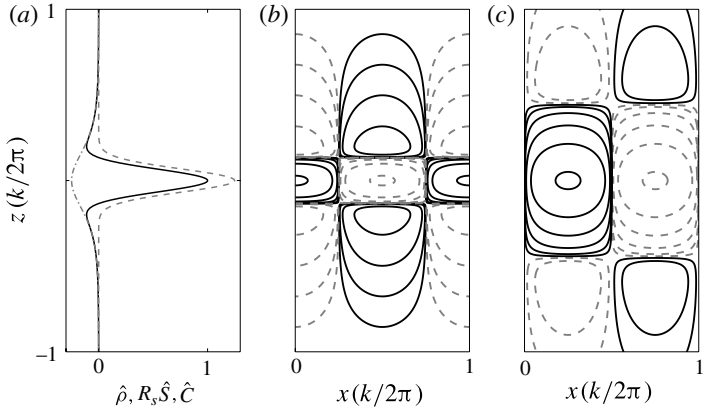


FIGURE 16. (*a*) The one-dimensional eigenfunctions of the total density (solid), particles (dashed) and salinity (dashed-dotted). (*b*,*c*) The two-dimensional eigenmodes of (*b*) density and (*c*) vorticity. The eigenmode contours are plotted using a logarithmic scale. The two local minima in the density eigenfunction are caused by the salinity perturbation being more diffuse than the particle one. Results for the most unstable mode with $Sc_s = 10^3$, $l_s = 0.2$ and $R_s = 2$.

the interfacial region. However, a significant difference is that the wavenumber of the most unstable perturbation is $k_{max} = 6.45$ while that of the classical RT case for $V_p = 0$ is $k_{max} \approx 0.4$. A second main difference is the presence of the weak upper and lower vorticity rolls. These rolls are caused by the density eigenmode possessing two local minima. These minima occur because the salinity eigenfunction is both more diffuse than the particle one and has the opposite sign.

https://doi.org/10.1017/jfm.2011.474 Published online by Cambridge University Press

5.2.3. *Scaling*

A primary goal of the current investigation lies in obtaining scaling relationships from the linear stability results, both for the rate at which the particles sediment out of river plumes, and for the dominant scales at which this sedimentation process occurs. Towards this end, we focus on the small-H regime, which corresponds to the important early stages of river plume dynamics. Furthermore, the results for $H = 0$ allow us to make connections with existing results for double diffusion in the absence of settling. Finally, double diffusive effects are primarily important during these early stages, whereas they lose their influence during the later phases, when the unstable layer thickness has grown large. The results for small H values in figures 10 and 12 suggest that σ_{max} and k_{max} strongly depend both on the ratio τ of the diffusion coefficients, and on the stability ratio R_s. While most modellers and experimentalists record the velocity of finite-amplitude fingers as a function of the governing parameters, this is not a quantity that we can obtain from a linear stability analysis. Hence, in the following we will use the maximum growth rate, σ_{max}, as a proxy for the finger velocity.

Experiments by Green (1987) and Parsons & Garcia (2000) analysed the scaling of the finger descent velocity in particle–temperature systems. Parsons & Garcia furthermore obtained a theoretical prediction for the steady-state finger velocity, by balancing the buoyancy gain as a result of the diffusion of heat/salinity into the finger with the buoyancy loss due to mixing and detrainment. Translating their relationship into our dimensionless variables, we obtain

$$W \propto Sc_s^{-1/3} R_s^{-2/3}. \tag{5.11}$$

Here, W is the finger descent velocity made dimensionless with the viscous velocity scale defined in (2.12). The experiments found an experimental value of -0.61 for the exponent of R_s, which is in good agreement with the expected results. However, no experiments were performed to verify the scaling with the diffusivity Sc_s.

The scaling of the finger width for salt fingers generated at a thin interface has been studied recently by Sreenivas *et al.* (2009). These authors applied a critical Rayleigh number criterion at the interface and found that the finger wavelength scaled with the Rayleigh number to the power $-1/3$. Very good agreement was observed between the theory and corresponding numerical calculations regarding the scaling with the stability ratio. On the other hand, the authors did not test their prediction for the scaling with the diffusion coefficient. Their relation, rewritten in the notation of this paper, is

$$k \propto Sc_s^{1/3} R_s^{1/3}. \tag{5.12}$$

Figure 17 shows the scaling behaviour of our linear stability results, along with the slopes predicted by the above theoretical arguments. The upper panels focus on the influence of the diffusivity of the stable, faster-diffusing component, with results being shown for three different stability ratios. We remark that we have chosen to look at the scaling as a function of Sc_s, rather than τ. We have performed additional calculations, not shown here, which show that, for $\tau > 20$ and a constant Sc_s, there is only a very weak influence of increasing τ. However, calculations that varied the value of Sc_s but held constant the value of $\tau = 100$ showed a strong dependence of both σ_{max} and k_{max} on Sc_s. This indicates that, once the salinity component is diffusing much faster than the particle component, the absolute rate of salinity diffusion, Sc_s, is important, rather than the relative rate of diffusion, τ. This is not to say that τ has become an unimportant quantity, however, as it is still very important when studying the effects of the stability ratio, as we will see shortly.

https://doi.org/10.1017/jfm.2011.474 Published online by Cambridge University Press

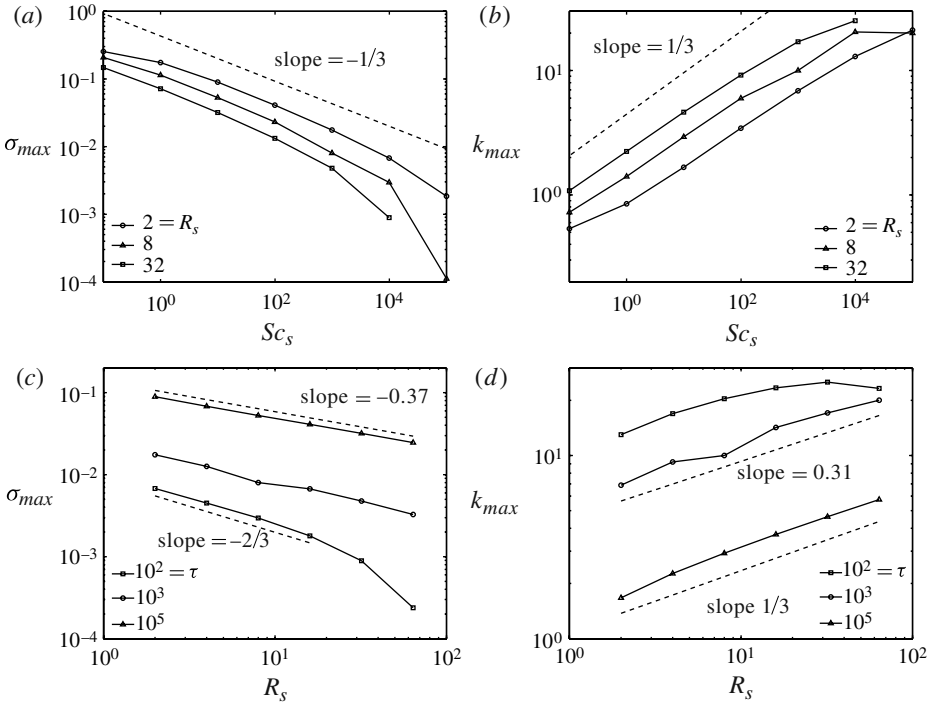


FIGURE 17. The scaling behaviour of (*a*,*c*) the maximum growth rate σ_{max} and (*b*,*d*) the wavenumber k_{max} against (*a*,*b*) the Schmidt number of the stable component and (*c*,*d*) the stability ratio. The solid lines represent data from our calculations while the dashed lines represent either the expected slope (fractions) or the best-fitting slope for trends that deviate from expectations (decimals). Calculations with $l_s = l_c = 0.4$, $Sc_c = 10^6$, $H = 0$ and $V_p = 0$.

Returning to figure 17 and starting with the maximum growth rate, σ_{max}, we see a good agreement with the 1/3 slope in the interior of the plot, while there are more substantial deviations on either ends. Similar to the maximum growth rate, the maximum wavenumber also exhibits good agreement in the interior of the domain, and poorer agreement at the two endpoints. At low values of Sc_s, the values of σ_{max} approach the limiting value of $\sim$0.3, especially for the $R_s = 2$ curve, and thus the curves begin to plateau. At the other extreme, the diffusion of the stable component is becoming so slow that the system is approaching a stable state. In fact, for $R_s = 32$ and $Sc_s = 10^5$, the system is stable, as it does not meet the criterion that $R_s < \tau^{3/2}$. With applications to river plumes in mind, the most important data points are those corresponding to $Sc_s = 7$ and 700, as those are the dimensionless values for temperature and salinity, respectively. From the plot, it is clear that double diffusive instabilities in a temperature–particle system have an approximately five times larger growth rate as compared to a salinity–particle one.

The lower two panels of figure 17 show the scaling behaviour of σ_{max} and k_{max} with the stability ratio R_s. Here we find more significant deviations from the above predictions. For the $\tau = 100$ curve, there is a strong drop in the maximum growth rate as $R_s \to \tau$. Although it was shown above that a double diffusive instability can occur for $R_s < \tau^{3/2}$, it seems that the growth rates show a strong decline long before this limit is reached. For smaller values of R_s, our best-fitting slope of -0.64 for $\tau = 10^2$

https://doi.org/10.1017/jfm.2011.474 Published online by Cambridge University Press

is very close to both the experimental observation of -0.61 and the theoretical value of $-2/3$ from Parsons & Garcia (2000). However, for the two larger values of τ, our numerical results have significantly lower best-fitting slopes of -0.48 and -0.37, respectively. It is worth noting that the experiments by Parsons & Garcia were for particle–temperature systems, and thus would have a very large τ. The differences in the scaling behaviour for different values of τ might possibly be attributable to the fact that the theoretical predictions are for the steady-state finger velocity, and not for the initial, linear growth rate. These two quantities are not necessarily interchangeable, as one is a measure of the initial growth of the instability, while the other one quantifies its strength during the later stages. However, both quantities do give information about the strength of the driving forces in the problem. While the reason for the dependence of the slope on τ is not entirely clear, it is important to know that the scaling exponent for the stability ratio depends on the diffusivity ratio. Interestingly, the behaviour of the maximum wavelength is almost exactly as predicted for both large and small τ, with the only deviations occurring when $R_s \approx \tau$.

5.3. *Influence of particle settling*

To lay the groundwork, § 4 analysed the influence of a settling velocity on the stability of a one-component diffusive system. Subsequently, § 5.2 focused separately on the influence of the salinity interface thickness and the unstable layer height in two-component systems, in the absence of a settling velocity. Based on the insight gained from these preliminary studies, we are now in a position to combine all of the above effects, and to address the stability properties of more realistic two-component base states in the presence of a settling velocity. Towards this end, we focus on the representative situation of a particle Schmidt number $Sc_c = 10^6$, in combination with a salinity Schmidt number $Sc_s = 7.0 \times 10^2$, so that $\tau = 1.4 \times 10^3$. We assume that the base state evolves from a mixed layer with $l_c = l_s = 0.1$ at time $t = 0$. For several distinct values of the settling velocity V_p, we subsequently compute the temporally evolving base states. Applying the QSSA, we then analyse the linear stability of these base states at various times.

We remark that these base states give rise to two distinct time-dependent length scales, *viz.* the salinity interface thickness l_s and the unstable layer thickness $H = V_p t$. Note that l_s grows diffusively, i.e. proportionally to $t^{1/2}$, while H grows linearly with t. Hence, for small times and settling velocities, the salinity interface may be thicker than the unstable layer, whereas the reverse is to be expected for large times and settling velocities. Earlier we introduced the ratio of the two length scales $R_t = V_p t/l_s$, whose influence we will now discuss in detail. By comparison, the particle interface thickness l_c remains approximately constant, as a result of the large particle Schmidt number. Depending on the settling velocity, one of two qualitatively different scenarios will evolve. For small settling velocities or small times ($R_t < 1$), the diffusive spreading of the salinity interface will outpace the convective growth of the unstable layer, so that the layer will largely remain embedded within the salinity interface. In this case, we expect double diffusive effects to dominate. For large settling velocities or large times ($R_t > 1$), on the other hand, the unstable layer thickness will grow more rapidly than the salinity interface thickness, and we anticipate that a Rayleigh–Taylor-like instability will develop at the particle interface.

The maximum growth rates shown in figure 18, along with the thickness ratio R_t, are consistent with these expectations. Here, the settling velocities span over two orders of magnitude, from $V_p = 0.0007$ on the far right to $V_p = 0.1829$ on the far left. We note that, for all settling velocities, the growth rate evolves in time from an

https://doi.org/10.1017/jfm.2011.474 Published online by Cambridge University Press

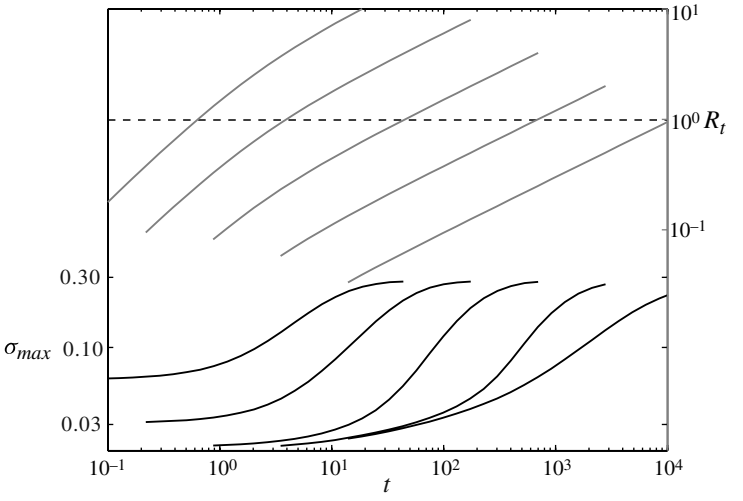


FIGURE 18. The most unstable growth rates (lower curves, left vertical axis) and the ratio (H/l_s) (upper curves, right vertical axis) for different snapshots of the base state in time. The five curves for both represent $V_p = (0.0007, 0.0029, 0.0114, 0.0457, 0.1829)$, from right to left. For larger settling velocities, the unstable layer thickness more quickly outgrows the salinity interface thickness. Calculations with $R_s = 2$ and $\tau = 1.4 \times 10^3$.

initial, lower plateau representing the double diffusive regime, to a final, higher plateau characteristic for the Rayleigh–Taylor regime. For the smallest settling velocity, the unstable layer remains embedded within the salinity interface up to $t \approx O(10^4)$. The initial growth rate of somewhat below 0.03 is consistent with the double diffusive value shown in figure 10 for $\tau = 10^3$, $R_t < 1$ and $V_p = 0$. For larger settling velocities, the initial growth rate is substantially higher, even though the unstable layer is still fully embedded within the salinity interface. This observation of increasing growth rates for larger settling velocities points at an interesting difference between two-component and single-component systems: for the latter, figure 7(*a*) had shown that the growth rate is independent of the settling velocity for $V_p < 1$, and decreases for $V_p > 1$.

For large times, all cases lead to $R_t > 1$, as the unstable layer eventually outgrows the salinity interface thickness, so that the unstable particle interface approaches the case of a single diffusive component with a settling velocity. Hence, consistent with the $V_p < 1$ regime shown in figure 7(*a*), the growth rates approach nearly identical asymptotic values of approximately 0.3 for all settling velocities. We note that, for small settling velocities, this asymptotic growth rate is approached already for $R_t \approx 1$. For larger settling velocities, on the other hand, by the time $R_t \approx 1$, the unstable layer thickness is still fairly small, so that the influence of the stable salinity interface reduces the growth rate of the Rayleigh–Taylor instability mode at the particle interface. Only for $R_t \gg 1$ does the salinity interface lose its stabilizing influence.

In figure 19 we examine the maximum growth rates against the two length scales l_s and H, for small and large settling velocities, respectively. For the lowest settling velocities, figure 19(*a*), the salinity interface thickness is the more important length scale, as was shown in figure 18. We note that, as the settling velocity increases, the behaviour of the maximum growth rate departs from the $V_p = 0$ case (dashed line) at

https://doi.org/10.1017/jfm.2011.474 Published online by Cambridge University Press

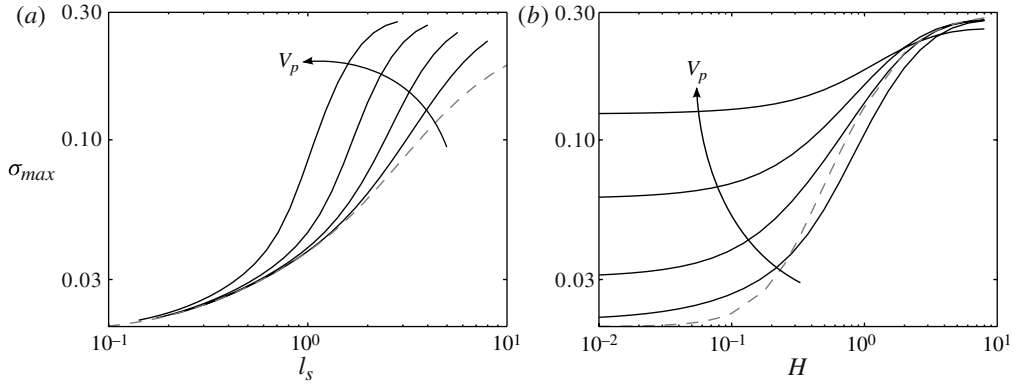


FIGURE 19. The maximum growth rates for (*a*) small and (*b*) large settling velocities are plotted against their respective important length scales. The dashed lines show results for $V_p = 0.0$. In both cases, the most unstable growth rate increases with increasing V_p. Calculations with $R_s = 2$, $\tau = 1.4 \times 10^3$ and (*a*) $V_p = (0.0007, 0.0014, 0.0029, 0.0057)$ and (*b*) $V_p = (0.0114, 0.0457, 0.1829, 0.7314)$.

earlier values of l_s. This departure reflects the influence of the unstable layer thickness, which becomes felt at smaller values of l_s for larger values of the settling velocity.

At higher settling velocities, the dominant length scale is the unstable layer thickness H. Figure 19(*b*) shows that, for larger settling velocities, the maximum growth rate increases from its initial plateau region at approximately $H = 0.1$ for all values of the settling velocity shown. This is consistent with the observations of figure 18 and indicates that the Rayleigh–Taylor mode begins to dominate over the double diffusive mode when the unstable layer thickness H exceeds a certain value. The dashed line again represents the $V_p = 0$ case according to figure 10(*a*). Here it does not represent a lower bound for the maximum growth rate, which may be due to the fact that for the calculations shown in figure 10 the salinity interface thickness was kept at the constant value of $l_s = 0.1$. Here, on the other hand, l_s grows with time, so that for the smallest settling velocities in figure 19(*b*) the salinity interface is thicker, which reduces the growth rate.

To better understand the interplay between the salinity interface thickness and the unstable layer height, we turn to the two-dimensional eigenfunctions shown in figure 20. The eigenfunctions for density (figure 20*a*,*b*), vorticity (figure 20*c*,*d*) and the streamfunction (figure 20*e*,*f*) are shown for $V_p = 0.0014$ (figure 20*a*,*c*,*e*) and 0.0457 (figure 20*b*,*d*,*f*). For the smaller settling velocity in panel (*a*), the density mode is only slightly shifted from the symmetry seen in the double diffusive instability shown in figure 16. The upper and lower rolls are caused by the salinity eigenfunction being more diffuse and opposite in sign to the particle one, similar to the eigenfunctions shown in figure 16(*a*,*b*). In contrast, figure 20(*b*) has the salinity perturbation clearly centred around the salinity interface, which provides a stabilizing influence on the particle perturbation that takes a form similar to the traditional RT instability. In addition to the density eigenfunctions, the vorticity ones shown in the middle row also provide insight into the dynamics of the instability. The small settling velocity has the main region of vorticity confined to a narrow central layer localized about the particle interface. Although the vertical extent of this region is small, it

https://doi.org/10.1017/jfm.2011.474 Published online by Cambridge University Press

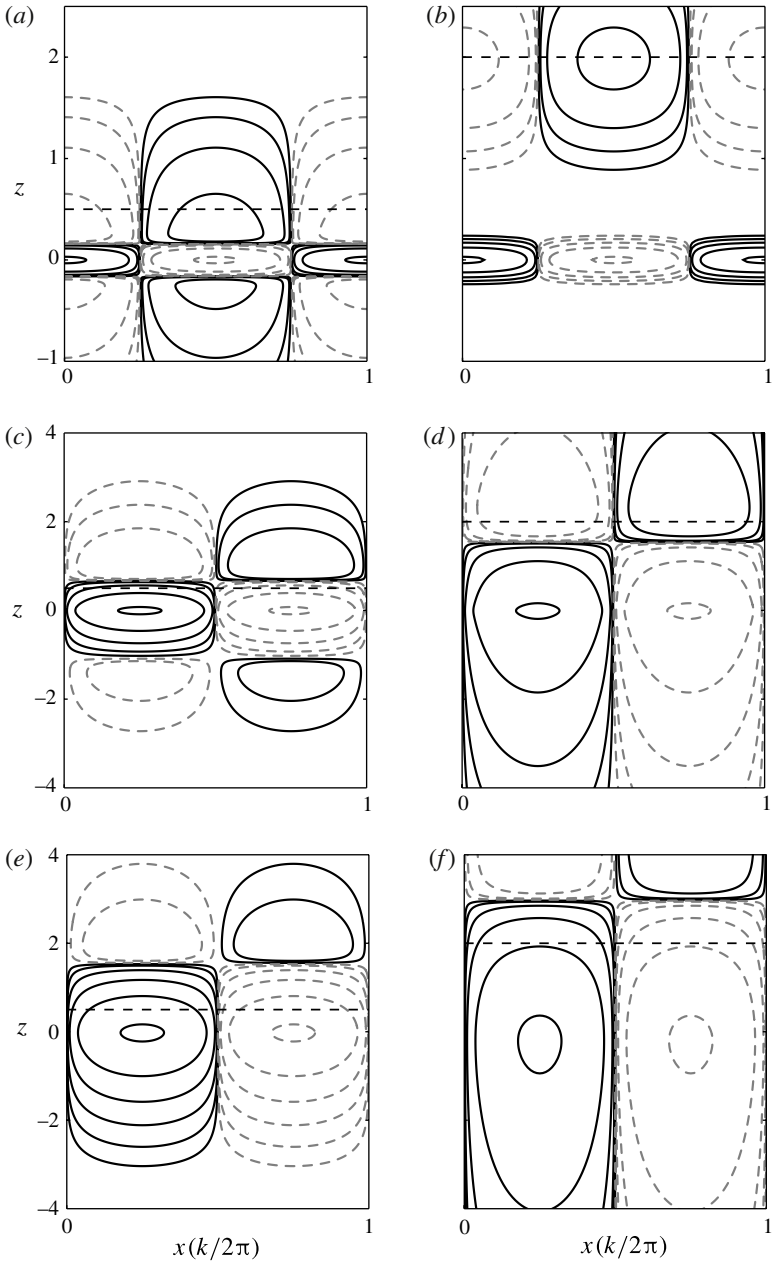


FIGURE 20. The two-dimensional eigenmodes for (*a*,*b*) density, (*c*,*d*) vorticity and (*e*,*f*) the streamfunction are shown for (*a*,*c*,*e*) $V_p = 0.0014$ and (*b*,*d*,*f*) $V_p = 0.0457$. The thickness ratios R_t are 0.36 and 4.0 for the panels, respectively. The contour values are plotted with a logarithmic scale between 0.001 and 0.9 and the horizontal dashed line represents the location of the salinity interface. Drastically different structures emerge, suggesting that different instability mechanisms are at play for different values of the settling velocity.

does extend above the salinity interface, which is indicated by the black dashed line. In the small settling velocity case, this leads us to believe that the salinity interface

https://doi.org/10.1017/jfm.2011.474 Published online by Cambridge University Press

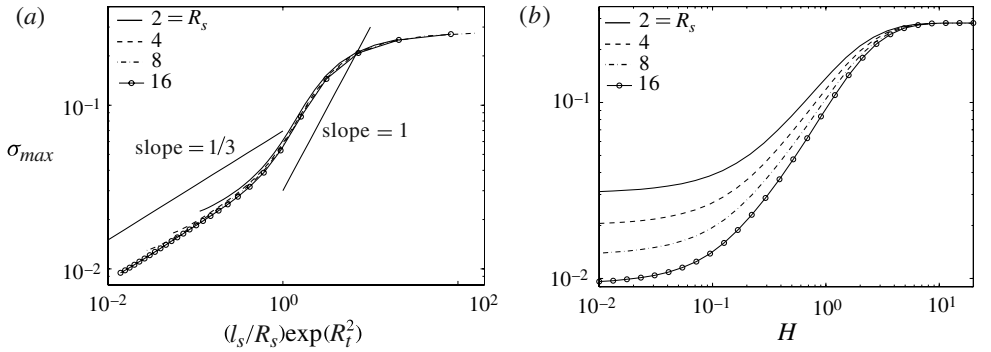


FIGURE 21. The maximum growth rate for four different values of the stability ratio, $R_s = (2,\ 4,\ 8,\ 16)$ and $\tau = 1.4 \times 10^3$. (*a*) $V_p = 0.0014$: in the small settling velocity regime, the growth rates for all R_s values collapse when plotted against the inverse salinity gradient. (*b*) $V_p = 0.0457$: the behaviour in the high settling velocity regime is very similar to the case with $V_p = 0$ and an imposed unstable layer thickness.

location is not as important to the instability as the salinity *gradient* at the particle interface, which was also found in § 5.2.2. Figure 20(*d*) is much different, with the main vorticity rolls being strongly confined by the presence of the salinity interface, with the interface itself outside of the main vortex rolls. Also, the rolls are much larger in size in figure 20(*d*) as compared to panel (*c*), which again points towards a more RT-type mode. Lastly, the bottom row of eigenfunctions shows the streamfunction $\hat{\psi}(z)$, which gives a visual for the actual motion of the fluid, whereas the vorticity only shows where rotation is being generated. In the small settling case, figure 20(*e*), the streamfunction is composed of two sets of rolls, with the top roll being very weak. This means that, while there were three layers of rolls in the vorticity eigenfunctions, the upper and lower ones are very weak and only influence the flow by confining the main roll to a more narrow central layer. In panel (*f*), the streamfunction of the higher settling velocity has the interesting feature that the lower rolls now extend beyond the salinity interface and into the region of fresh water. The vorticity contours had the main set of rolls terminate below the salinity interface. This fact is interesting because it means that, even with an RT-type mode, the instability at higher settling velocities will bring fresh water down to the saline region.

Figure 21 shows the effect of varying the stability ratio, R_s, on the maximum growth rates for two different settling velocities. As in figure 15, the small settling velocity regime in figure 15(*a*) is plotted against the inverse of the salinity gradient δ_s at the location $z = 0$, where $\delta_s = (l_s/R_s)\exp(R_t^2)$. The curves for all values of R_s are seen to collapse, which indicates that the dominant parameter in the small settling velocity regime is the strength of the salinity gradient at the particle interface. This observation is consistent with the collapse seen in the $V_p = 0$ limit, figure 15, and in the shape of the eigenfunctions examined in figure 20(*a*,*c*,*e*). The shape of the curve can be separated into three regions based on the inverse salinity gradient δ_s. For $\delta_s < 1$, the maximum growth rate increases as $\delta_s^{1/3}$. For δ_s values somewhat larger than unity, we observe $\sigma \propto \delta_s$. For $\delta_s \gg 1$, the particle interface has essentially moved away from the salinity gradient, so that it can develop a Rayleigh–Taylor-like instability that is unaffected by the salinity gradient. As a result, the growth rate levels off in this regime. Overall, the different regimes in figure 21 reflect the dual role of the salinity:

https://doi.org/10.1017/jfm.2011.474 Published online by Cambridge University Press

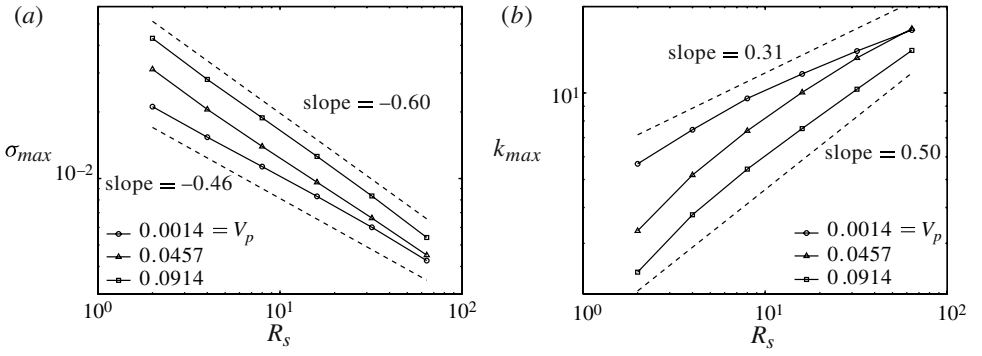


FIGURE 22. (*a*) The maximum growth rate and (*b*) wavenumber as a function of the stability ratio for different values of the settling velocity. The results show a slope that is dependent on the settling velocity as well as a possible shift in the mode of the instability. The dashed lines show the range of slopes between curves. Calculations with $Sc_s = 700$, $Sc_c = 10^6$, $l_s = l_c = 0.4$ and $H = 0$.

on the one hand, it makes double diffusion possible, and, on the other, it can retard the Rayleigh–Taylor instability for moderate unstable layer thicknesses.

The large settling velocity regime shown in figure 21(*b*) is very similar to figure 12 for an imposed unstable layer thickness and $V_p = 0$. For thin unstable layers, larger stabilizing salinity gradients are seen to reduce the growth rates. For thick unstable layers, the stable salinity interface loses its influence no matter how large R_s is, and the situation approaches that of a particles-only system.

5.3.1. *Scaling and experimental comparisons*

Previously, we looked at scaling relationships for the maximum growth rate and wavenumber in the absence of a settling velocity. There, the focus was on the influence of the Schmidt number of the faster-diffusing component, Sc_s, and the stability ratio, R_s. In this section, we will keep Sc_s constant and will instead focus on the stability ratio and the settling velocity V_p. Figure 22 plots σ_{max} and k_{max} against the stability ratio R_s. We recognize a weak dependence of the curves on the settling velocities. In the plot of the maximum growth rate, the slowest settling velocity shown has a slope of -0.46, while that of the largest settling velocity is closer to -0.60. This may seem counter-intuitive, as we might expect the theory to be more accurate for smaller settling velocities. However, figure 17 shows that for larger τ values the best-fitting slope is less than the theoretically predicted value of $-2/3$. This effect, combined with the apparent increase in the slope due to the settling velocity, causes the largest settling velocity curve to have a slope closest to the predicted value of $-2/3$. It is important to note that, at small to moderate stability ratios, the lowest settling velocity shown in figure 22 undergoes more of a double diffusive instability while the two larger ones undergo an RT-type instability. One possible explanation for the difference in slopes is that, at large stability ratios, the double diffusive instability is strongly damped by the stable salinity profile and the mode switches to an RT-type one. This idea is supported by the fact that the wavenumbers for the two different settling velocities are approximately the same at the largest stability ratio shown. We remark that the wavenumber plot also shows different slopes based on the settling velocity.

https://doi.org/10.1017/jfm.2011.474 Published online by Cambridge University Press

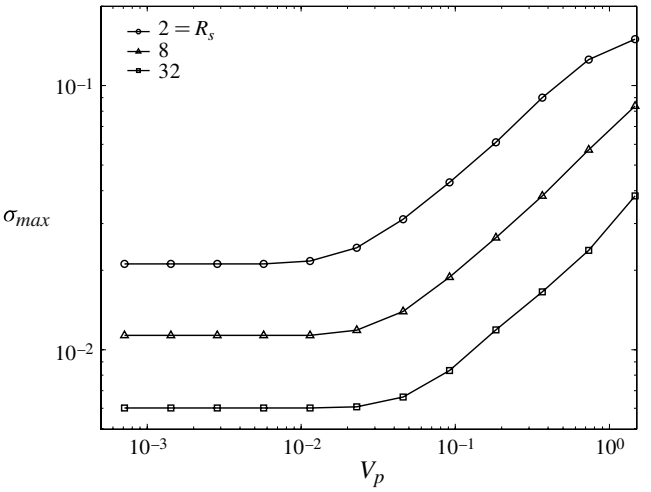


FIGURE 23. The maximum growth rate as a function of the settling velocity at $H = 0$ for three different stability ratios. Calculations with $Sc_c = 10^6$, $Sc_s = 700$, $H = 0$ and $l_s = l_c = 0.4$.

A practically important question concerns the influence of the grain size on the instability growth rate during the early stages, when the unstable layer is still thin. Figure 23 summarizes our results for $H = 0$. The three solid lines represent the maximum growth rate for three different stability ratios. For small settling velocities V_p, the instability grows on a fast time scale, as compared to the particle settling process. As a result, the unstable layer thickness varies slowly, and the QSSA approximation should be valid. In this regime, we find that the growth rate is largely independent of the settling velocity. For large settling velocities, on the other hand, the growth rate increases strongly with the settling velocity. However, in this parameter regime the QSSA approximation becomes increasingly questionable, and it will be desirable to supplement the present investigation by fully nonlinear, unsteady simulations.

We are now in a position where we can undertake qualitative comparisons with the experiments performed by Parsons *et al.* (2001). Those authors considered particle-laden fresh water above particle-free saline water, with the two layers initially kept separate by a thin divider. While in most of the experiments the two layers also had different temperatures, we will initially focus on those experiments without a temperature difference. The details of the 15 experiments in this category can be found in table 2 of Parsons *et al.* (2001), and are provided in table 1 in the notation of the present paper. We recognize a general trend for fingering to occur at low values of the stability ratio, while leaking dominates at higher values. In terms of the modes discussed in this paper, we saw that, at small values of the stability ratio R_s, double diffusive instabilities tend to dominate, while at larger stability ratios, the dominant mode switches to the Rayleigh–Taylor type. In figure 23, increases in the stability ratio are seen to reduce the growth rates. This means that the instability is slow to develop and the unstable layer will have time to grow. Taken together with the results of figure 21, which show that for thicker unstable layers the instability becomes more Rayleigh–Taylor-like, we can begin to understand the general trend of table 1. Note, however, that in experiment 16 the stability ratio is still quite low and yet the instability type has become an intermediate of fingering and leaking. In this case, the

https://doi.org/10.1017/jfm.2011.474 Published online by Cambridge University Press

Exp no.	R_s	V_p	Type	Exp no.	R_s	V_p	Type
82	2.8	1.3×10^{-2}	Fingering	7	11.8	5.6×10^{-1}	Intermediate
16	4.9	5.1×10^{-1}	Intermediate	8	11.8	1.2×10^{-2}	Leaking
9	5.3	9.9×10^{-3}	Leaking	97	11.8	1.0×10^{-1}	Leaking
43	5.9	9.3×10^{-3}	Intermediate	110	11.8	2.5×10^{-1}	Leaking
33	7.1	9.9×10^{-3}	Intermediate	80	14.2	1.3×10^{-2}	Leaking
93	7.8	1.3×10^{-2}	Leaking	35	35.4	1.7×10^{-2}	Leaking
31	8.8	1.1×10^{-2}	Intermediate	47	70.8	2.1×10^{-2}	Leaking
92	11.3	1.3×10^{-2}	Intermediate				

TABLE 1. Data from Parsons *et al.* (2001) converted into the notation of this paper. These data points were chosen because $\Delta T = 0$. We explain the general trend of going from fingering to leaking based on whether the instability is double diffusive or Rayleigh–Taylor based.

settling velocity is quite large, which according to § 5.3 favours a Rayleigh–Taylor-type instability mode. While the above arguments do not fully explain every single data point in the table, such as for example experiments 9 and 93, they do capture the general trend.

Interestingly, among the experiments by Parsons *et al.* (2001) there were three cases without salinity difference, but with a stabilizing temperature difference instead. In all of these cases, fingering was seen to dominate even though the stability ratio ranged from 5.3 to 23.0. We believe that this can be accounted for by the fact that the much faster diffusion of temperature (as opposed to salinity) favours double diffusive instability, and thus results in the fingering mode. Taken together, the above observations suggest that double diffusive instability modes result in the fingering mode observed by Parsons *et al.* (2001), while leaking is more closely related to the Rayleigh–Taylor instability.

6. Summary and conclusions

The present investigation sheds light on the instability mechanisms that govern the sedimentation of particles from buoyant river plumes. In particular, the role of double diffusion during the early stages of this process is clarified.

The linear stability results demonstrate that the interactions between the particle and salinity concentration fields can be quite complex. In the absence of salinity, particle settling is seen to dampen the growth of the Rayleigh–Taylor instability at the boundary separating the particle-laden fluid from the clear fluid below. This damping effect is a result of the smearing of the vorticity field, which in turn is caused by the clinging of vorticity to the fluid elements as the interface between clear and particle-laden fluid passes through. An important quantity is the ratio of the particle settling velocity to the viscous velocity scale of the instability growth. As long as this ratio is small, particle settling has a negligible influence on the instability growth. However, when the particles settle more rapidly than the vorticity layer diffuses, the growth rate decreases inversely proportional to the settling velocity.

In the presence of a stably stratified salinity field, this picture changes dramatically. An important new parameter is the thickness H of the unstable layer that contains both salt and particles. As long as this unstable layer thickness is smaller than, or of the same magnitude as, the thickness of the diffuse salinity interface, double diffusive

https://doi.org/10.1017/jfm.2011.474 Published online by Cambridge University Press

effects strongly influence the sedimentation dynamics. For unstable layer heights much larger than the salinity interface thickness, the particle and salinity interfaces become increasingly decoupled, so that the dominant instability mode is of Rayleigh–Taylor type, centred at the lower boundary of the particle-laden flow region.

For thin unstable layers, double diffusive effects are seen to destabilize statically stable density distributions, while modifying the most amplified wavenumber by up to an order of magnitude. In contrast to the situation without salinity, particle settling can have a *destabilizing* effect and significantly increase the growth rate, even in the limit of vanishing unstable layer thickness. An analysis of the eigenfunctions provides insight into the structure of the dominant convection rolls.

The present linear stability results are largely consistent with scaling results proposed by other authors. Specifically, we find that, over a wide range of salinity Schmidt numbers, the growth rate scales as $Sc_s^{-1/3}$, consistent with the theoretical arguments put forward by Parsons & Garcia (2000). The most amplified wavenumber behaves as $Sc_s^{1/3}$, which agrees with the predictions by Sreenivas *et al.* (2009). With regard to the stability ratio R_s, the linear stability results confirm the scaling proposed by Parsons & Garcia (2000) of $R_s^{-2/3}$ for the finger descent velocity only for small diffusivity ratios. For larger diffusivity ratios, the linear stability results show an exponent closer to $-1/3$. On the other hand, the linear stability results show a dependence of the most amplified wavenumber as $R_s^{1/3}$, as predicted by Sreenivas *et al.* (2009). Increasing settling velocities are seen to lead to a stronger dependence of the growth rate and the dominant wavenumber on R_s

We remark that one needs to be cautious, of course, when trying to obtain scaling laws for the propagation velocity of nonlinear, finite-amplitude fingers from linear stability results. With that in mind, the overall level of agreement observed above is perhaps better than what one might have expected. A second issue concerns the assumption of a quasi-steady base state made for the purpose of conducting the linear stability analysis. Especially for larger settling velocities, the unstable layer thickness may vary on a time scale that is comparable to that of the instability growth. For this reason, it will be important to extend the present investigation into the nonlinear regime, by means of unsteady, high-resolution numerical simulations. Efforts in this direction are currently under way.

Acknowledgements

The authors would like to thank Professor T. Maxworthy and Dr L. Lesshafft for helpful and stimulating discussions. This research was supported by NSF grants CBET-0854338, CBET-1067847 and OCE-1061300.

REFERENCES

ALISEDA, A., CARTELLIER, A., HAINAUX, F. & LASHERAS, J. C. 2002 Effect of preferential concentration on the settling velocity of heavy particles in homogeneous isotropic turbulence. *J. Fluid Mech.* **468**, 77–105.

BATCHELOR, G. K. & NITSCHE, J. M. 1991 Instability of stationary unbounded stratified fluid. *J. Fluid Mech.* **227**, 357–391.

BERRUT, J. P. & MITTELMANN, H. D. 2004 Adaptive point shifts in rational approximation with optimized denominator. *J. Comput. Appl. Maths* **164–165**, 81–92.

BERRUT, J. P. & TREFETHEN, L. N. 2004 Barycentric Lagrange interpolation. *SIAM Rev.* **46**, 501–517.

BLANCHETTE, F. & BUSH, J. W. M. 2005 Particle concentration evolution and sedimentation-induced instabilities in a stably stratified environment. *Phys. Fluids* **17**, 073302.

https://doi.org/10.1017/jfm.2011.474 Published online by Cambridge University Press

BOSSE, T., KLEISER, L. & MEIBURG, E. 2006 Small particles in homogeneous turbulence: settling velocity enhancement by two-way coupling. *Phys. Fluids* **18**, 027102.

CHANDLER, F. 1998 The convective instability of fluid interfaces. PhD thesis, University of Southern California.

CHANDRASEKHAR, S. 1961 *Hydrodynamic and Hydromagnetic Stability*. Oxford University Press.

CUETO-FELGUEROSO, L. & JUANES, R. 2009 Adaptive rational spectral methods for the linear stability analysis of nonlinear fourth-order problems. *J. Comput. Phys.* **228**, 6536–6552.

GRAF, F., MEIBURG, E. & HÄRTEL, C. 2002 Density-driven instabilites of miscible fluids in a Hele–Shaw cell: linear stability analysis of the three-dimensional Stokes equations. *J. Fluid Mech.* **451**, 261–282.

GREEN, T. 1987 The importance of double diffusion to the settling of suspended material. *Sedimentology* **34**, 319–331.

HENNIGER, R., KLEISER, L. & MEIBURG, E. 2010 Direct numerical simulations of particle transport in a model estuary. *J. Turbul.* **11**, 1–31.

HILL, P., SYVITSKI, J. P. M., COWAN, E. & POWELL, R. 1998 In situ observations of floc settling velocities in Glacier Bay, Alaska. *Mar. Geol.* **145**, 85–94.

HOYAL, D. C., BURSIK, M. I. & ATKINSON, J. F. 1999*a* The influence of diffusive convection on sedimentation from buoyant plumes. *Mar. Geol.* **159**, 205–220.

HOYAL, D. C., BURSIK, M. I. & ATKINSON, J. F. 1999*b* Settling-driven convection: a mechanism of sedimentation from stratified fluids. *J. Geophys. Res.* **104**, 7953–7966.

HUPPERT, H. E. & MANINS, P. C. 1973 Limiting conditions for salt-fingering at an interface. *Deep-Sea Res.* **20**, 315–323.

HUPPERT, H. E. & TURNER, J. S. 1981 Double-diffusve convection. *J. Fluid Mech.* **106**, 299–329.

LELE, S. K. 1992 Compact finite difference schemes with spectral-like resolution. *J. Comput. Phys.* **103**, 16–42.

LINDEN, P. F. & SHIRTCLIFFE, T. G. L. 1978 The diffusive interface in double-diffusive convection. *J. Fluid Mech.* **87**, 417–432.

MAXWORTHY, T. 1999 The dynamics of sedimenting surface gravity currents. *J. Fluid Mech.* **392**, 27–44.

MCCOOL, W. W. & PARSONS, J. D. 2004 Sedimentation from buoyant fine-grained suspensions. *Cont. Shelf Res.* **24**, 1129–1142s.

MEIBURG, E. & KNELLER, B. 2010 Turbidity currents and their deposits. *Annu. Rev. Fluid Mech.* **42**, 135–156.

MILLIMAN, J. D. & SYVITSKI, J. P. M. 1992 Geomorphic/tectonic control of sediment discharge to the ocean: the importance of small mountainous rivers. *J. Geol.* **100**, 525–544.

NECKER, F., HÄRTEL, C., KLEISER, L. & MEIBURG, E. 2002 High resolution simulations of particle-driven gravity currents. *Intl J. Multiphase Flow* **28**, 279–300.

PARSONS, J. D., BUSH, J. W. M. & SYVITSKI, J. P. M. 2001 Hyperpycnal plume formation from riverine outflows with small sediment concentrations. *Sedimentology* **48**, 465–478.

PARSONS, J. D. & GARCIA, M. H. 2000 Enhanced sediment scavenging due to double-diffusive convection. *J. Sedim. Res.* **70**, 47–52.

PHARO, C. H. & CARMACK, E. C. 1979 Sedimentation processes in a short residence-time intermontane lake, Kamloops Lake, British Columbia. *Sedimentology* **26**, 523–541.

RADKO, T. & STERN, M. 2000 Finite-amplitude salt fingers in a vertically bounded layer. *J. Fluid Mech.* **425**, 133–160.

REDEKOPP, L. 2002 Elements of instability theory for environmental flows. In *Environmental Stratified Flows* (ed. R. Grimshaw), pp. 223–281. Kluwer Academic.

SCHMITT, R. 1979 The growth rate of super-critical salt fingers. *Deep-Sea Res.* **26A**, 23–40.

SREENIVAS, K., SINGH, O. & SRINIVASAN, J. 2009 On the relationship between finger width, velocity, and fluxes in thermohaline convection. *Phys. Fluids* **21**, 026601.

https://doi.org/10.1017/jfm.2011.474 Published online by Cambridge University Press

STERN, M. 1969 Collective instability of salt fingers. *J. Fluid Mech.* **35**, 209–218.

SYVITSKI, J. P. M., ASPREY, K., CLATTENBURG, D. & HODGE, G. 1985 The prodelta environment of a fjord: suspended particle dynamics. *Sedimentology* **32**, 83–107.

TEE, T. W. & TREFETHEN, L. N. 2006 A rational spectral collocation method with adaptively transformed Chebyshev grid points. *SIAM J. Sci. Comput.* **28** (5), 1798–1811.

TURNER, J. S. 1967 Salt fingers across a density interface. *Deep-Sea Res.* **14**, 599–611.

TURNER, J. S. 1973 *Buoyancy Effects in Fluids*. Cambridge University Press.

WEIMER, P. & SLATT, R. M. 2007 *Introduction to the Petroleum Geology of Deepwater Setting*. *AAPG Studies in Geology*, American Association of Petroleum Geologists.

WRIGHT, L. D. & COLEMAN, J. M. 1974 Mississippi River mouth processes: effluent dynamics and morphologic development. *J. Geol.* **82** (6), 751–778.

https://doi.org/10.1017/jfm.2011.474 Published online by Cambridge University Press